NOAA Technical Report ERL 373-WPL 47

Implementation of Coastal Current-Mapping HF Radar System Progress Report No. 1

D.E. Barrick
M.W. Evans
July 1976

Implementation of Coastal Current-Mapping HF Radar System Progress Report No. 1

D.E. Barrick
M.W. Evans

Wave Propagation Laboratory
Boulder, Colorado

July 1976

NOTICE

The Environmental Research Laboratories do not approve,
recommend, or endorse any proprietary product or proprietary
material mentioned in this publication. No reference shall
be made to the Environmental Research Laboratories or to this
publication furnished by the Environmental Research Labora-
tories in any advertising or sales promotion which would in-
dicate or imply that the Environmental Research Laboratories
approve, recommend, or endorse any proprietary product or
proprietary material mentioned herein, or which has as its
purpose an intent to cause directly or indirectly the adver-
tised product to be used or purchased because of this Envi-
ronmental Research Laboratories publication.

FOREWORD

This report was written to serve a variety of users. The project has
been sponsored over the past eighteen months by the National Oceanic and
Atmospheric Administration (NOAA), the Outer Continental Shelf Environmental
Assessment Program (OCSEAP), the U.S. Coast Guard, and the Energy Research
and Development Administration (ERDA). Each of these sponsors has its
own reporting requirements — typically 4-6 page summaries issued at
specified periods and in a specified format — and hence we cannot hope
to describe the technical content of our developmental program in those
reports. Therefore, the present document is not specifically a sponsor
report.

On the other hand, many within the remote-sensing community, the
oceanographic community, from universities, institutes, and private
industry have been requesting technical details on the system we are
developing. Up to now, no formal publication has been prepared on our
radar system for the applications intended here, even though the physics
behind the scatter process have been analyzed in the various research
papers cited in our report. This report is therefore the first in a
series, intended to supply technical details to our many scientific
colleagues who have been patiently awaiting further information on our
system.

A single reader having a given technical area of specialization will
undoubtedly find certain sections easy, while other sections will be diffi-
cult or even incomprehensible without additional background reading. A
reader who desires a cursory understanding of the sea-scatter physics,
fundamentals of the operation of our system, its capabilities, limitations,
and expected performance should read Sections 1, 2, and 6. One interested
in the engineering details of the hardware should read Section 3. Discussion
of digital system software — both the software written to control the
operation of the radar and the software written to mathematically process
the sea-echo signals — is undertaken in Section 4. A technical specialist
who wants the detailed mathematics behind the operation of the radar and
signal processing should concentrate on Sections 4.3 and 5. Finally,
the systems analyst who desires details of the mathematics behind our
projected system performance and optimizations should read Section 5.

CONTENTS

IMPLEMENTATION OF COASTAL CURRENT-MAPPING HF RADAR SYSTEM
PROGRESS REPORT NO. 1

D. E. Barrick and M. W. Evans

A concept for radar remote-sensing of near-surface ocean currents in coastal regions is described, and progress is reviewed on the design and construction of the first operational units. The system employs pairs of low-power (50 W), transportable, HF (30 MHz) radars whose signals from the shore are scattered from ocean waves that serve as tracers, i.e., underlying currents impart a slight change in velocity to the ocean waves, which is detected by the radar receiver. Signals from each of the two geographically separated radar units of the pair, scattered from the same point on the sea, are used to construct a complete current vector for that point. In an operational system a radar pair will take simultaneous measurements over an ocean area with a grid having a 3-km spacing. Vectors will be constructed for each 3-km-square section, and a map of the near-surface current field will be output in real-time by a mini-computer on-site. All radar and digital gear is contained in two shock-mounted fiberglass cases, only 44 inches high and weighing under 200 pounds. The radar antennas are easily erectable frames holding three vertical aluminum pipes; the entire system can be set up in less than an hour. All of the individual components of the system have been designed and constructed. The system software has been essentially completed and checked out in the laboratory. Only a small amount of final assembly remains to be done before checkout and use in the field. System performance and simulation studies show that a radar pair can provide current data to a range from the coast of about 70 km. The optimum spacing between paired radars is nominally 40 km. Error analyses show that probable azimuthal position errors are less than 3° for signal-to-noise ratios exceeding 10 dB. Simulations using random sea-echo and noise signals indicate that probable rms current-velocity errors are not more than 5 cm/s.

1. INTRODUCTION

1.1 The Need

Surface currents are defined as the mean horizontal flow of water within the uppermost layer of the ocean. The thickness of this layer can be nominally taken as 20 to 50 centimeters. On the open oceans, the heights of the waves present will almost always be many times greater than the thickness of this top layer; in addition, the phase velocities of these waves will also be much larger than the speeds of the mean surface currents (e.g., 10 to 100 times greater). Because of these two facts, the moored current meter — which is used successfully at greater depths — is relatively useless for measuring surface currents.

Yet the currents in the uppermost layer of the ocean are of great importance, especially in near-coastal regions. Anything that floats on the surface is transported by these currents, waves notwithstanding. (The wind may also impart some velocity component to an object with appreciable vertical surface area above the water.) Thus the trajectory and fate of an oil spill or a leak from an offshore rig will depend upon the patterns of the near-surface currents in the area, as will the destination of hot water and pollutant effluents discharged near the shore. And the rescue of a person in the water, especially in conditions of poor visibility, could be aided considerably by real-time observations of surface currents over the area and relevant trajectory predictions.

The Bureau of Land Management (BLM), the Energy Research and Development Administration (ERDA), the U.S. Coast Guard, and private oil companies are expending a great deal of resources to assess the impact on the environment of massive offshore oil operations. Although a wide spectrum of scientific disciplines must be involved in such investigations, the underlying question of paramount importance in all of these studies is: Where does floating oil released near a drilling platform go? The transport of pollutants, whether in toward shore or out to sea, will depend upon many factors, such as winds, waves, storms, tides, the coastline contour, and geophysical forces such as gravity and the Coriolis force (due to Earth rotation). Thus near-surface offshore currents will be highly variable from area to area and at different times. While the ultimate objective is to predict these currents as a function of the driving forces, their accurate measurement is the necessary first step in the development and testing of such a prediction model. In fact, when the near-surface currents are known, it is theoretically possible to (numerically) calculate the currents and circulation all the way to the ocean floor.

Yet these near-surface currents are the most difficult to measure. Nearly all available techniques are Lagrangian in nature, meaning that they measure the trajectory of a parcel of water near the surface, thus obtaining one or more (current) streamlines vs. time. The most common technique consists of visually or photographically observing a dye marker's dispersal or the movement of timed-release floats from an airplane. Such experiments are expensive and hence limited in area and time. Drogued free-floating

buoys, tracked either by radar or optically (from land, ship, and possibly in the future by satellite) represent an alternative technique. Satellite tracking of several such buoys will ultimately provide valuable information on general oceanic circulation patterns and thence, surface wind and ocean/ atmosphere energy exchange, but can hardly be useful for the finer grid-scale requirements for coastal waters over the continental shelves.

2. AN HF RADAR SYSTEM FOR MEASURING SURFACE CURRENTS

Approximately two years ago, we identified a remote-sensing concept that appears to be ideally suited to measuring near-surface currents in coastal areas. The system we have designed and developed uses two HF shore-based transportable radars to measure current patterns, and it provides, in real time, a map-like record of the currents. These currents are determined for 3 km x 3 km areas of ocean out to 70 km from shore, and are displayed at the centers of each such area within a rectangular grid.

2.1 Sea-Scatter Physics

The mechanism behind the radar under construction here — permitting the measurement of near-surface currents — involves the physics of scatter from ocean waves. Ocean waves (and one in particular) are the "target" for the radar system. Since this target is moving, it produces a "Doppler shift" on the received echo; this merely means that the signal returns at a slightly different frequency than that transmitted, because of the radial rate of closure of the target. The radar receiver/processor measures this Doppler shift, and this permits the determination of the radial component of the current velocity by the following process. The ocean wave motion — producing the measured Doppler shift — consists of two linear combinations of velocity. One is due to the "intrinsic" velocity of any deep-water gravity surface wave; from hydrodynamic theory, this phase velocity to first order is precisely $v_{ph} = \sqrt{gL/2\pi}$, where $g \simeq 9.81$ ms^{-2} (the acceleration of gravity), and L is the wavelength of the water wavetrain. The second velocity component of the wave is due to the current; it is as though the wave were being transported in a Cartesian coordinate system attached to the mean water transport. Thus, by measuring the total Doppler shift (and hence the total radial ocean-wave velocity), and precisely knowing the first component (due to the intrinsic wave velocity), one determines the second term, which is the desired radial component of surface current.

The logical question at this point is: How does one know precisely which wavetrain out of the entire spectrum constituting the ocean surface is doing the scattering? The physical mechanism behind HF scatter from the sea was discovered over twenty years ago by Crombie [1955]. By looking at ocean waves with a shore-based HF radar and spectrally analyzing the received echoes, he observed two dominant "spikes" or peaks, symmetrically spaced about the carrier frequency (Fig. 1). These spikes indicated that of all the randomly time-varying ocean waves being observed by the radar,
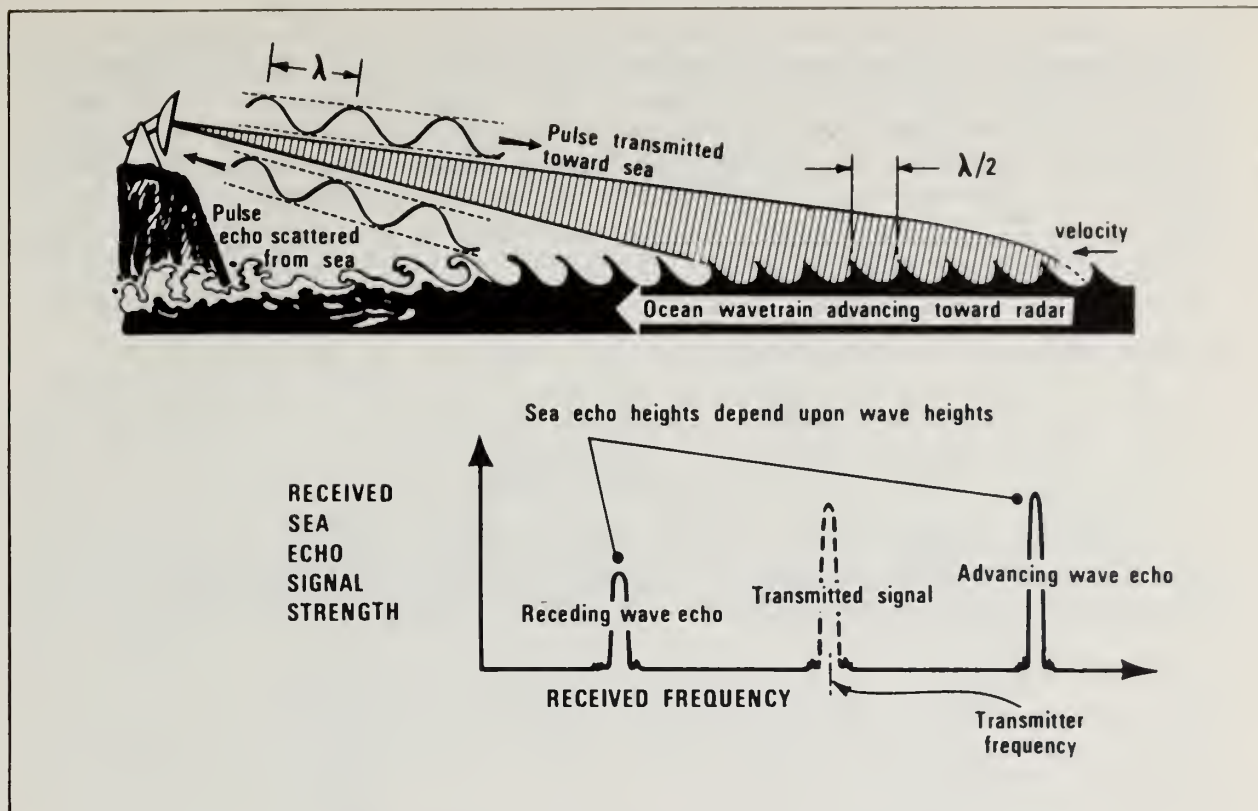
Figure 1. Sketch of first-order Bragg-scattering process
and schematic of sea-echo Doppler spectrum.

only two sets were significant (to first order), just as though two dis-
crete targets were producing all of the scatter. By deducing the velocity
of these "target" ocean waves from their symmetrical Doppler shifts, and
thence the wavelength of the scattering wavetrains, he found that the
wavelength was precisely one-half the radar wavelength (for backscatter at
grazing incidence along the sea). This is shown schematically in Fig. 1.
Thus Bragg scatter — or the diffraction-grating effect — is the respon-
sible interaction mechanism. Therefore, out of all the wavetrains present
on the ocean surface, only the two wavetrains (or gratings) with a period
precisely one-half the radar wavelength and moving radially toward and away
from the radar produce the scatter. Crombie confirmed this explanation
experimentally by noting that the unique "square-root" relationship between
this Doppler shift and the radar carrier frequency followed the square-root
water-wave dispersion relationship (between its phase velocity and its
wavelength). A theoretical study [Wait, 1966] based upon a deterministic,
periodic sea surface, and a different study [Barrick, 1972a] based upon a
random sea-surface description both confirmed the empirically discovered
scatter mechanism and also gave expressions for the echo amplitude.

Crombie also first observed [Crombie, et al., 1970] that these echo
peaks are often offset by a discrete amount from their symmetrical positions
about the carrier frequency. This is illustrated in the measurements made
from San Clemente Island and reported elsewhere [Barrick et al., 1974].

3

Fig. 2 shows a typical sample spectrum observed at 9.4 MHz. In these measurements, Δ represents the normalized Doppler-offset contribution due to the radial component of the near-surface currents, where ± 1 are the expected (normalized) positions of the first-order peaks. Thus, the radial component of current is deduced from such a radar record using the equation $v_{cr} = \Delta \cdot v_{ph}$, where v_{ph} ($= \sqrt{g\lambda/4\pi}$) is the phase velocity of the first-order Bragg-scattering waves (λ being the radar wavelength, $= c/f_o$, where c is the free-space radio wave velocity and f_o is the carrier frequency). For the case shown in Fig. 2, $v_{cr} = 22.5$ cm/s in the direction toward the radar, using these relationships.

2.2 Background

Crombie [Crombie et al., 1970; Barrick et al., 1974] and Stewart and Joy [1974] have been studying radar-deduced near-surface currents, both theoretically and experimentally. In Barrick et al., [1974], Crombie shows
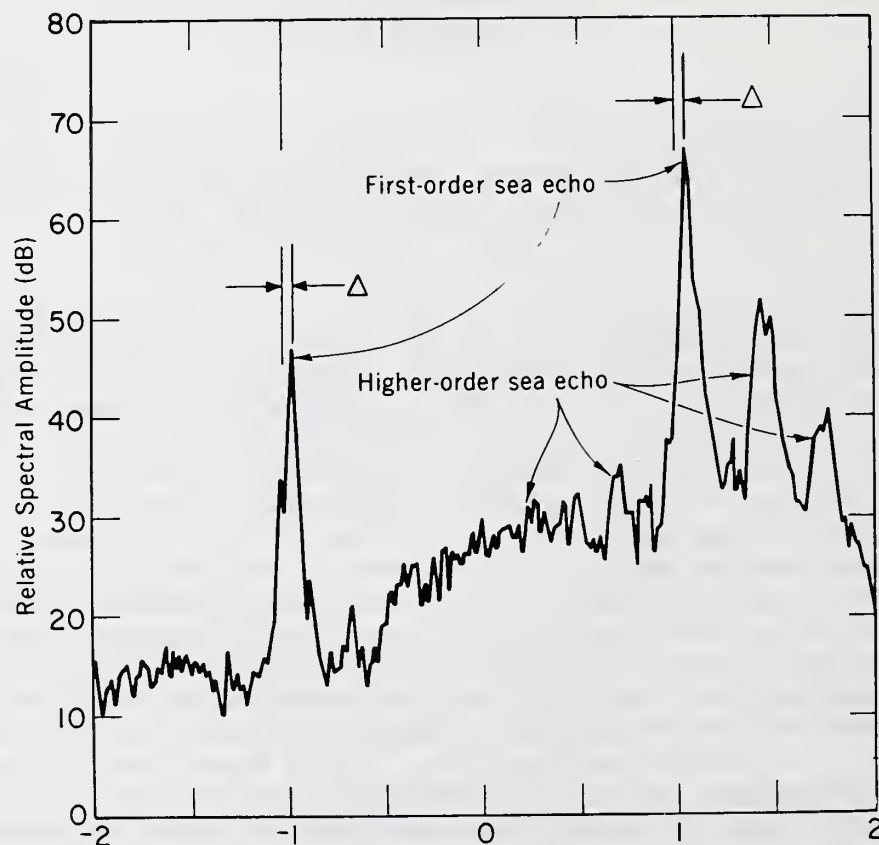
Figure 2. Typical 9-sample average of 200-second surface-wave HF sea-echo power spectra at 9.4 MHz. Doppler frequency is normalized with respect to the expected position of the first-order Bragg peaks (here 0.313 Hz); Δ is the normalized shift of the record due to an underlying current. Narrow-beam radar is looking due west from San Clemente Island.

4

that the depths of the current flow that influence the Doppler offset produced by first-order scatter from the Bragg wavetrain lie within one twenty-fifth radar wavelength of the mean water surface. Hence to measure currents even closer to the surface, one would use a shorter-wavelength (higher-frequency) radar. At 30 MHz, for example, currents to a depth of about one foot would be detected by first-order Bragg scatter. Since the currents closest to the surface are most responsive to atmospheric driving forces — as well as being the most difficult to measure — our present system is designed to radiate near 30 MHz.

Besides theoretical analyses, several experiments have already been performed to prove that not only is the concept feasible, but also sufficient accuracy is possible that a powerful but simple remote-sensing tool based on this concept can be developed. Both Crombie [in Barrick et al., 1974] and Stewart and Joy [1974] have shown that the radial component of surface current can be measured to a reasonable precision; we cite results from the latter reference here. Using the joint NOAA/NAVY surface-wave radar facility on San Clemente Island and a drogue buoy operated by Scripps, verification of the concept was obtained. The buoy — drogued to drift with currents at a mean depth of about one meter — was tracked by a microwave radar as it drifted across the area observed by the HF radar, as shown in Fig. 3. The observing radar had a directional antenna that could look simultaneously in the two directions shown; many frequencies could also be utilized simultaneously. Fig. 4 shows the actual geographic track of the
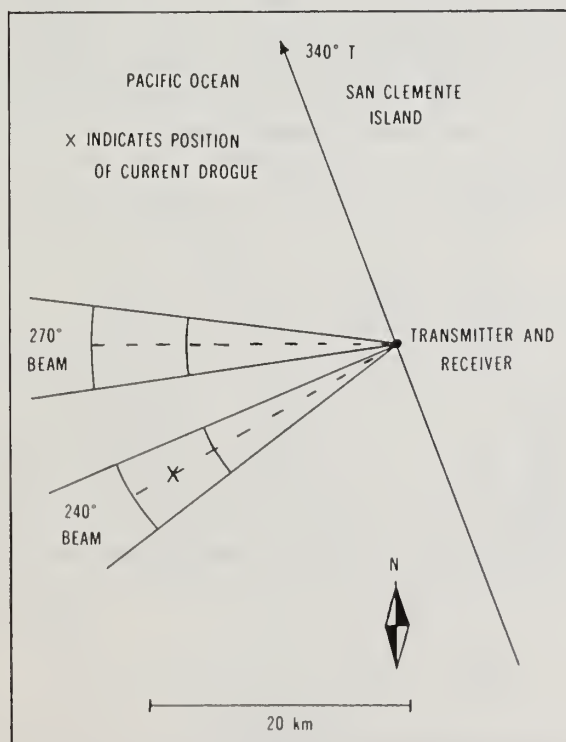

Figure 3. Configuration of HF surface-wave radar and its two beams on San Clemente Island. "X" shows initial position of drifting buoy.
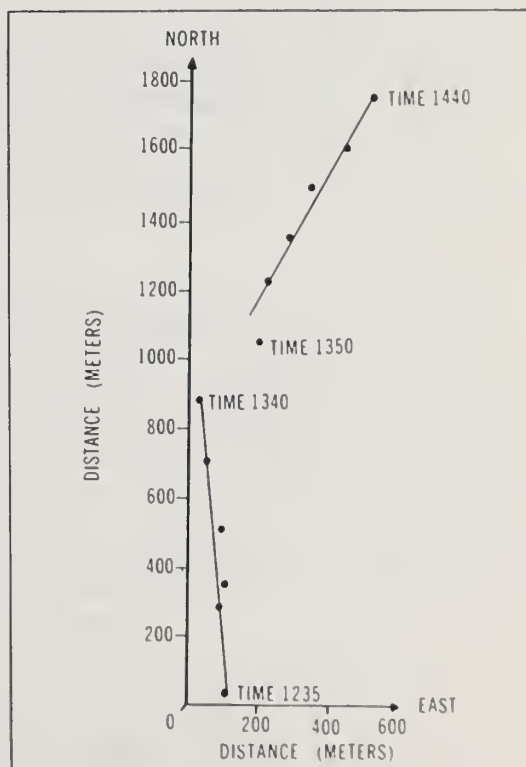
Figure 4. Drift of drogued buoy vs. time, starting at 1235 on 24 May 1972 at "X" shown in Fig. 3

5

buoy (on May 24, 1973) vs. time, starting from the "X" in Fig. 3 at 1235. The current vectors radial to the HF radar along the two beam directions were deduced from this plot. Since this current — at a mean depth of one meter — would (according to the theory) be sensed by an HF radar at a frequency of 12 MHz, this mean radial velocity of the buoy was plotted in Figs. 5 and 6 at that frequency as the circle-dot; the other points are the radar-deduced radial current speeds. The error bars on the current speeds correspond to a Doppler resolution of 0.005 Hz (requiring a 200-second coherent integration time). The buoy currents compare favorably with the radar-deduced currents. Also, it is expected that the currents very near the surface will be the greatest, since they are influenced most by the atmosphere. Under such a current shear, the higher radar frequencies should "see" greater currents than lower radar frequencies; this phenomenon is reflected in the plots of observed current vs. radar frequency shown in these figures.

Figure 5.   Radar-deduced radial current velocities along the two beams compared with buoy measurements.

Figure 6.   Radar-deduced radial current velocities along the two beams compared with buoy measurements.

6

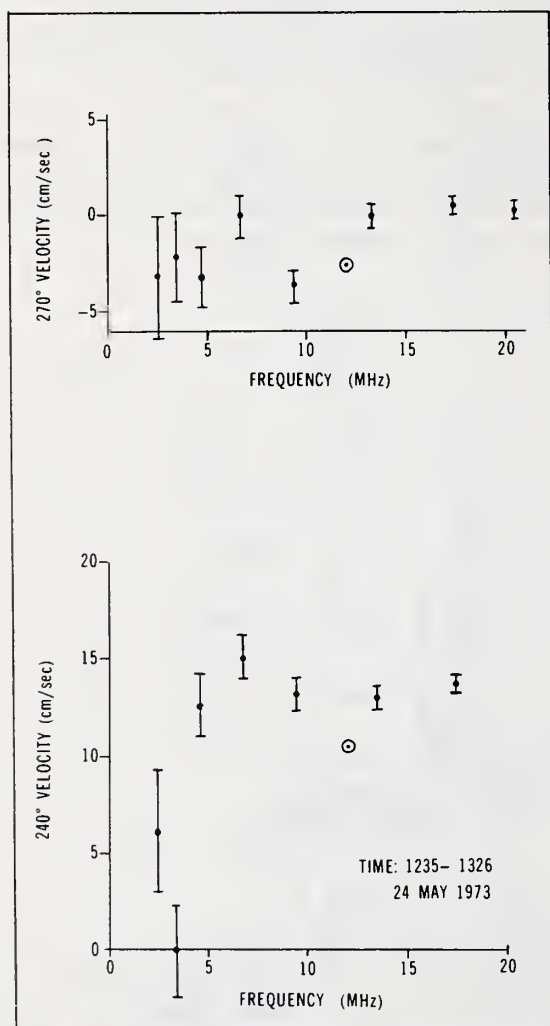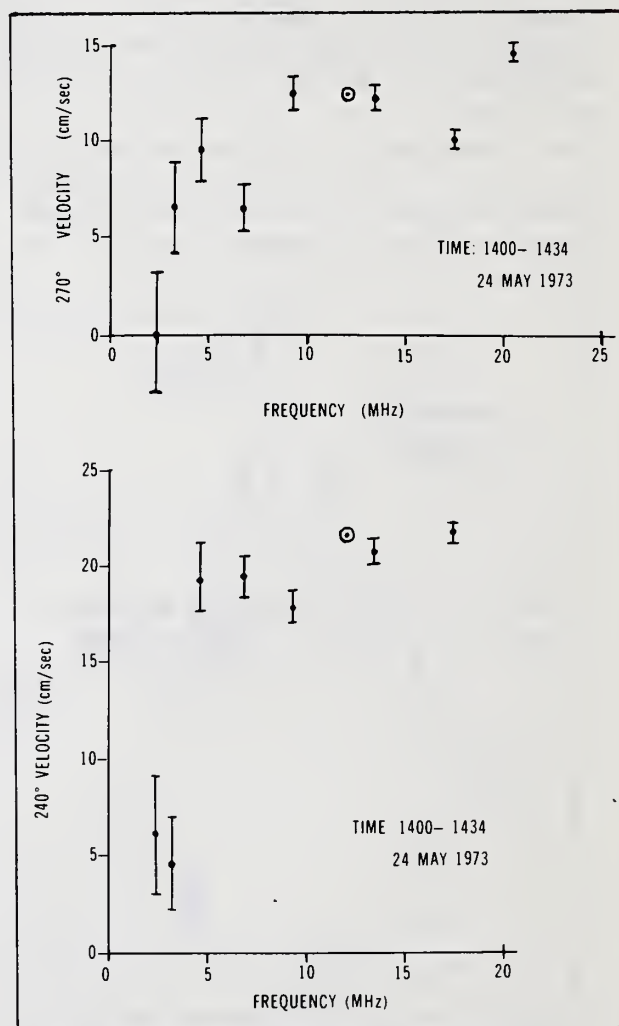Our transportable radar under construction here differs from the San Clemente Island radar used in the above experiment in the method by which the azimuthal direction-of-arrival of the sea-scattered signal is determined. The San Clemente Island radar used the "brute-force" approach of employing a long antenna array (about 800 ft) to form a fairly narrow azimuthal beam. The system under development here, on the other hand, measures this direction of arrival by comparing the phase difference of the scattered signal at two or more closely spaced simple antenna elements (i.e., about 15 feet apart). Although in principle it should be possible to sort out the directions-of-arrival of signals having differing Doppler shifts, the development of an operational station pair based upon this rather novel concept should have some preliminary experimental verification. Crombie et al. [1970] in fact performed such an experiment, in which they used two simple receiving antennas in Florida near Cape Kennedy to look east across the Gulf Stream. The concept was thus tested against the well-known gross features of the Gulf Stream in its south-to-north flow. For a semicircular radar resolution cell (corresponding to a given echo time delay) the current to the south should produce positive Doppler shifts (with respect to the expected first-order Doppler position); the currents to the east, zero relative Doppler shift; the currents to the north, a negative relative Doppler shift. By measuring the echo phase difference, $\Phi(\Delta f)$, between both antennas at each Doppler shift, Δf, from the first-order peak, α, we should be able to determine the direction-of-arrival from the equation $\Phi = k_o \, d \sin \alpha$, where d is the (known) spacing between the two receiving antennas, and k_o is the (known) radar wavenumber, given by $2\pi/\lambda$, λ being the radar wavelength. This correspondence between Δf, Φ, and α is illustrated in typical measurements at 6.92 MHz, shown in Fig. 7. The "spreading" of the normally narrow first-order Doppler peaks by the strong current is shown at the top, where the positive Doppler peak is seen to be stronger. The phase difference, Φ, is plotted on the lower portion, and one can see the expected correspondence between the direction-of-arrival and Doppler shift (from the center of the first-order peaks).

Hence, research experiments have already demonstrated the validity of the concepts underlying the radar system under development. These prior experiments were research efforts, in the sense that data were recorded in the field and analyzed later. The present development program is aimed at: (i) building a transportable, turn-key system that can produce its final near-real-time output in the field, viz, a current-vector map; and (ii) determining the accuracy of the system in terms of range/azimuthal resolution and current velocity measurement precision. Hence, the development of operational units is the next logical step in the progression of a new remote-sensing concept from the research stage to the routine operational stage.

2.3 Description of the Concept

In order to construct a map of current vectors representing water transport near the surface, radar sea-echo signal must be processed in a special manner. Signals are needed from two coastal stations (separated
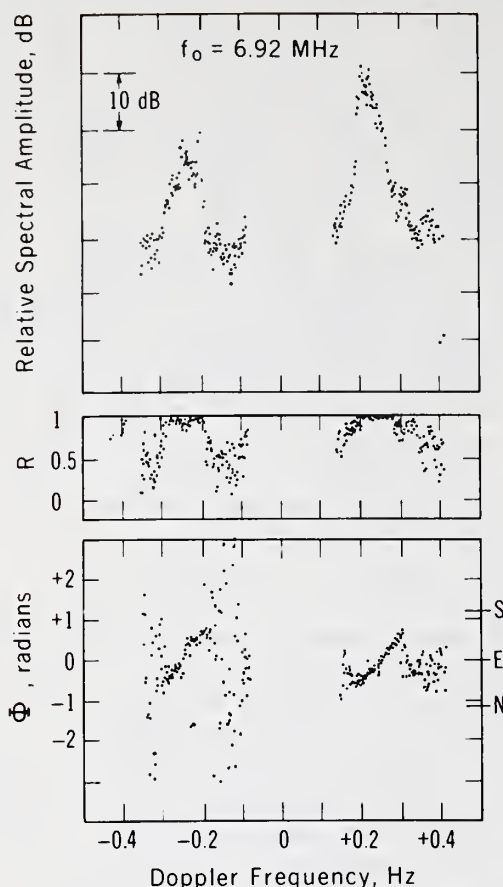
7

Figure 7. Upper: Doppler spectrum of current-smeared sea echo from Gulf Stream received by omni-directional antenna.

Middle: Normalized magnitude of coherence function between two antennas for these spectra.

Lower: Phase of coherence function between two antennas for these spectra (after Crombie et al., 1970).

by tens of kilometers) are required to obtain a complete horizontal vector at any point, since those from one station alone can provide only the current-vector component radial to that station.

Three basic quantities, then, are needed from two stations to produce a current map: (i) the range to the point at which the current vector is desired; (ii) the azimuthal angle to the grid point from a specified direction; (iii) the radial component of current velocity. The first two quantities pinpoint the geographical source of the echo, and the third represents the desired geophysical quantity to be extracted from the echo. The range, or distance, to the scattering point (or cell) is determined from the two-way propagation time of the signal; in other words, the time of pulse transmission is noted, and the time of receipt of the echo thereafter is directly proportional to the distance of the scattering patch from the radar. In the system being constructed, this echo sampling vs. time after transmission is done digitally, and the sequential time samples are referred to as "range gates". The radial width of a given range-gated scattering cell, called the range resolution, is directly proportional to the transmitted pulse width; for the pulse width of 20 μs to be used here, the corresponding range resolution is 3 km. A given range resolution cell is

in reality a circular annulus; in all, approximately 24 range gates will be employed to give a maximum range from each station of $\sim$ 75 km.

The signal received from each range gate therefore represents the echo from an entire semicircle of sea (assuming the semicircle behind the radar lies over land). The azimuthal direction of arrival of the signal within a given range gate is determined from the phase difference between the signals received at multiple antennas at the same echo Doppler shift. For two antennas parallel to the beach, this phase (at a given Doppler shift from the first-order echo, Δf), is $\Phi(\Delta f) = k_o d \sin \alpha(\Delta f)$, where $k_o = 2\pi/\lambda$ (λ is the radar wavelength), d is the distance between the two antennas, and $\alpha(\Delta f)$ is the angle-of-arrival from the perpendicular to the beach/baseline. In order that the relationship between α and Φ be unambiguous as α goes from -90° to +90°, it is necessary that d be less than $\lambda/2$. At 30 MHz (λ = 10 meters) for example, this spacing should be 5 meters or less. The phase comparison is done by digital computer after the echo from a given range gate has been digitized.

The use of two receiving antennas can provide unambiguous direction of arrival only if the Doppler shifts due to the current from each point in the semicircular range-resolution cell are different. Such an assumption may not represent the actual current pattern under observation. A uniform current flow parallel to the beach, for example, will produce a different, unique, Doppler shift for each point on the semicircular scattering cell. A uniform current flow perpendicular to the beach, however, will produce a double-valued Doppler pattern, and with only two antennas, it will not be possible to distinguish the echo signal at $-\alpha_1$ from that at $+\alpha_1$. This double-valued ambiguity can be resolved, however, by using three receiving antennas and solving two sets of equations (digitally) in two unknowns. Likewise, a triple-valued current-pattern ambiguity can be resolved by using four receiving antennas. Since double-valued current patterns are considered possible, whereas triple (and greater) valued functions are considered much less likely, the presently planned system will use three receiving antennas 2-1/2 meters apart, arranged in a straight line. If initial field observations frequently show higher-valued current ambiguities, appropriate expansion of the receiving antenna system will be undertaken to handle these situations.

The range and azimuth (and hence the grid-point position on the map) of a given sea-echo signal samplehaving been determined, the current-vector component at that point oriented in the direction of the radar is obtained from the Doppler frequency shift, Δf, from the expected first-order echo position, f_B, as $v_{1,2}^r = \lambda \Delta f_{1,2}/2$ ($f_B = \sqrt{g/\pi\lambda}$, with g $\simeq$ 9.81 ms^{-2}), where the subscripts refer to the radar station at which the observations are made. Then the total current vector at that point is then determined on the computer as the trigonometric combination of the two radial components for the given grid point.

The hardware and software components required to perform all of the radar control, transmission, reception, and signal processing functions will be described in greater detail in subsequent sections of this report.

As an introduction to the overall design and operation, the actual flow of a signal through the system based upon the block diagram of Fig. 8 will be traced briefly here.

The receiver is the most complex and costly piece of hardware in the system; it performs several functions, including the synthesis of the desired radar operating frequency and the generation of the transmitted RF pulse. A system timing circuit — or "clock" — generates all of the timing signals used in the system. In particular, it generates a digital 10 MHz bit stream and digital pulsing/gating signals (20 μs wide, at a 1 kHz rate) and sends both sets of signals to the receiver. There the synthesizer divides the 10 MHz stream down, and then multiplies it back up again to arrive at the system operating frequency (between 25 and 35 MHz) selected by the operator. The pulsing signals from the clock are also used to form a low-level (10-dBm) RF pulse every millisecond at the selected operating frequency. This analog pulse stream is the basic transmitted signal; it is sent through the transmitter-driver where it is amplified to a 50-W peak-power level matched to a 50 Ω impedance. After power-splitting, amplification through four identical solid-state power amplifiers, and a recombination process, the pulse signals are radiated at 2.4 kW peak (or ∿ 48-W average level) through a semi-directive vertically-polarized Yagi
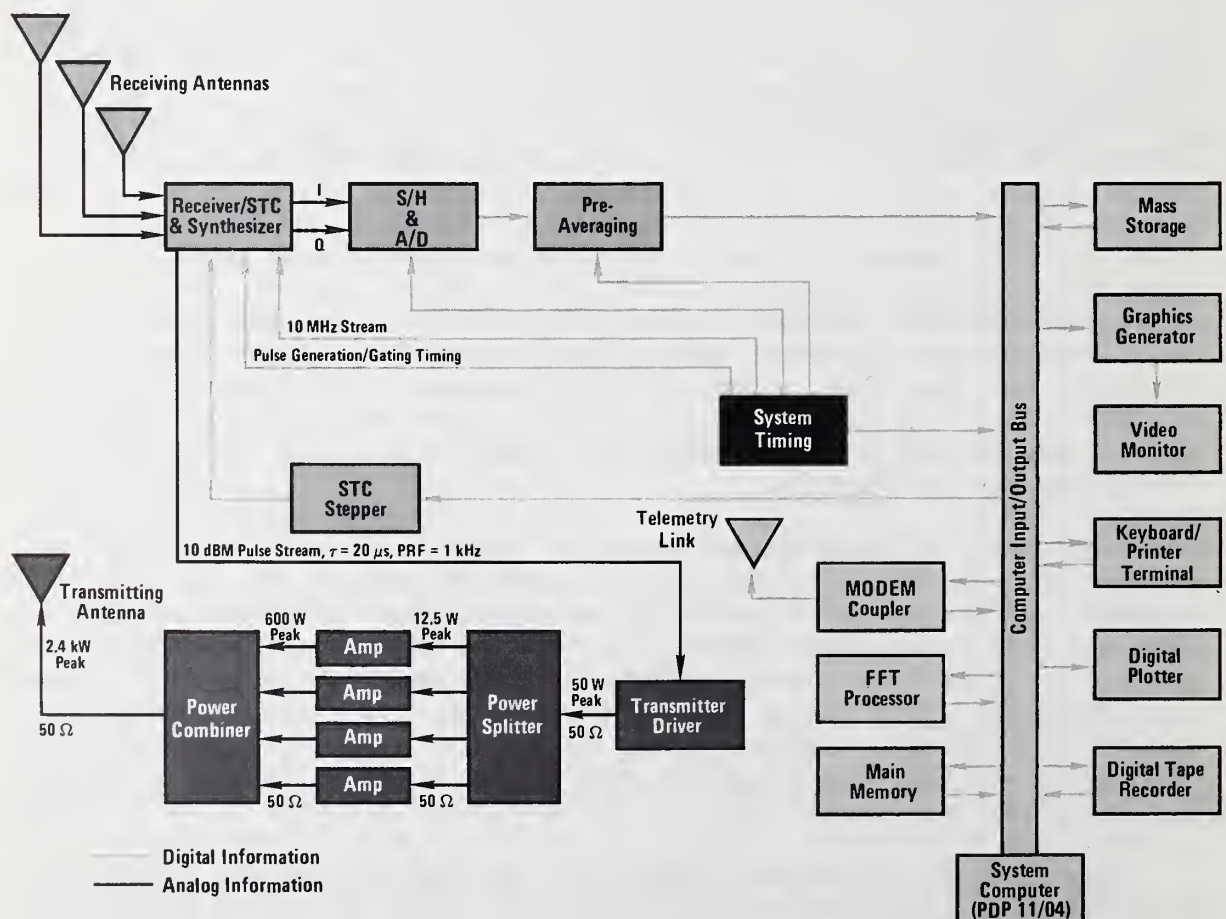

Figure 8.   Overall block diagram of current-mapping radar system.

monopole antenna array. All components in the transmitter/antenna chain are matched to 50 Ω for maximum power transfer.

During the time of pulse radiation, the receiver is switched off by the timing signals to prevent burnout and then switched back on to receive the sea-scattered echoes. These echo signals are received on three simple, short vertical whip antennas designed to have very high (nearly infinite) input impedance. No attempt is made to "match" impedances at the receiver input because the predominant noise in the system is external noise (at < 30 MHz), and hence a low-noise-factor receiver front end achieved through careful matching and balancing is not required. In addition, short high-impedance antenna elements keep the antenna currents very low, minimizing the undesired effects of mutual coupling between receiver antenna elements and also with the transmitter antenna. Both the transmitter and receiver antennas are simple elements only a few feet high that can be erected in a matter of minutes.

In actuality, only one receiving antenna is connected to the receiver at a time. In other words, immediately after the transmitter pulse is radiated, antenna #1 will be connected to the receiver input by the pulse timing signals. This antenna will remain connected to the receiver until the echo from the most distant patch of sea has been received (i.e., about 0.7 millisecond after transmission). Then antennas #2 and #3 are each sequentially connected to the receiver for similar periods, after which the process is repeated. The receiver also obtains digital signals from the sensitivity-time control (STC) stepper. This causes attenuation of various levels to be inserted in the receiver IF gain stages in a pre-programmed manner. Since the maximum signals will be received immediately after transmission, because of the extremely strong echoes scattered at short ranges, the attenuation vs. time after pulse transmission decreases monotonically. This STC function is necessary to prevent saturation and undesired nonlinear effects that would occur, since the desired echo-signal dynamic range would greatly exceed the dynamic range of the analog-to-digital convertor if compensation for range were not made.

The receiver forms an IF signal in the normal manner by mixing the RF signal with a local oscillator signal generated by the synthesizer. Two IF channels are employed: an "in-phase" channel (designated I) and "quadrature" channel (designated Q). The signals through these channels are "balanced" to have the same amplitude, but are 90° out of phase with each other. This is one of the two usual methods employed when Fourier transformation of the signal is ultimately to be performed; it allows the signal to be mixed to a "zero-IF" before digitization, after which the signals from each channel form the real and imaginary arrays of the Fourier transform input. The Fourier transform output then contains signal power at both negative and positive Doppler shifts near DC.

The zero (or baseband) IF signals out of the receiver have an information content approximately 1 Hertz in bandwidth (because of the nature of the sea echo), even though the actual signal bandwidth is much greater. These analog signals are "sampled and held" (S/H) every 10 µs (the aperture time is less than 2.0 ns, during which the signals are constant). These signals are then digitized, and from this point on, all processing is

11

digital in nature. Even though the signals are digitized every 10 μs, only every other sample is ultimately used; these alternate digital samples thus each represent sea echo from consecutive 20 μs range gates. Only the signals from the first 32 range gates after every pulse transmission are retained for processing, even though there are actually fifty 20 μs time intervals available between consecutive pulse transmissions. Since consecutive pulses are received sequentially on each of the three antennas, it takes 3 ms for the signal on a given antenna to be sampled again. Hence 3 x 32 = 96 total samples for both the I and the Q channels are obtained every 3 ms.

These signal samples then pass through a digital component that pre-averages them for one-half second. In other words, for the I channel and antenna #1 and, say, range gate #7, two samples arriving every 3 ms for a total of one-half second are added together to form an averaged signal. Thus the digitization process (at a one-third kHz rate per range gate per antenna) and the pre-averaging process effectively reduce the signal band-width to 2 Hz (i.e., -1 Hz to + 1 Hz), or about twice its intrinsic value for ultimate processing. For each of the 32 range gates, for each of the three antennas, and for both the I and the Q channels, there are therefore 167 (rounded from 166 2/3) pulses averaged to form 32 x 3 x 2 = 192 digital samples every half second. Each of these 192 samples being obtained every 0.5 second is stored in a memory component for a total of 256 seconds until a total of 192 x 256/0.5 = 98,304 samples are collected. At the end of 256 seconds, each of the 96 I and Q channels has produced a time-series array of 512 digital samples, and these then ultimately become the real and imaginary parts of the input to the fast-Fourier transform (FFT) processor. Therefore as many as 96 complex Fourier transforms, each of 512-word length, must be calculated every 256 seconds in order for the system computer to keep up with the data input, or to work in "real-time"; this will in fact be accomplished with the system under construction with no difficulty.

The computer input/output bus serves as the transfer point between digital hardware components for the processing of all digital data. After FFT processing, the data arrays are ready for the mathematical algorithms that extract the radial current velocity at each of the predetermined set of grid points (roughly 3 x 3 km apart). The echo signal-to-noise ratio is checked at each Doppler frequency shift for each range gate and antenna; if it does not exceed a predetermined threshold, the signal sample is discarded. If the signal-to-noise ratio exceeds the threshold, the azimuthal angle-of-arrival is extracted from the three antenna samples at each Doppler frequency, and a running average over several 256-second samples is computed. For each range gate, a curve is fit to the data points giving Doppler frequency vs. azimuthal angle-of-arrival. Each grid point on the desired map is then converted to range and azimuth angle for each radar location. Interpolation procedures are used to find the proper range gate samples; then from the digital "curve" or array of Doppler frequency vs. azimuth angle, the Doppler is found at the desired grid point. From this, the radial current velocity at that grid point is found. These radial current velocity values are then stored until they can be combined trigonometrically with those from the second site to produce the final output, a current-vector map. The total radar operating time required to produce one such map could range

12

from five minutes to two hours, depending upon a number of factors; the optimum measurement time should ultimately be selected only after field experience.

3.   SYSTEM HARDWARE

3.1   Digital Components

This section presents a brief description of the properties and functions (as they are seen at the present state of progress) of various digital components of the current-sensing-radar system, as configured in the block diagram of Fig. 8.   In some cases, two or more devices represented functionally as a single block in that figure are actually combined constructionally on a single chassis board.   Certain of the devices to be described here have been designed and constructed "in-house"; others have been purchased from commercial sources.   Nearly all of the digital hardware that is to be employed with the system in the field is to fit in one (of two) weatherproof fiberglass cases containing shock-mounted racks.   Fig. 9 is a photo of the total field system at one site, with the digital gear contained primarily in the left case and the RF gear in the right case; each case is 40" high x 24" wide and will weigh less than 200 pounds, capable of being handled by two persons.

Each of the major digital hardware items is described below:

Figure 9.   Current-sensing-radar components mounted
in their fiberglass cases for field use.

3.1.1 A/D Hardware & System Timing Module

Three functions represented in Fig. 8 have been combined into a single hardware module: (i) the sample and hold (S/H) and analog-to-digital convertor (A/D) functions; (ii) the pre-averaging function; and (iii) the system timing function. This module has been designed and assembled in-house; a photo of the module is shown in Fig. 10, and a block diagram is shown in Fig. 11.

The S/H and A/D convertors represent the first digital component in the signal flow through the receiver chain. Two analog signals are output from the receiver into this device, one each from the I (in-phase) and Q (quadrature) channels; these signals are "zero-IF" (centered on DC or zero frequency) with a bandwidth of approximately 50 kHz (the reciprocal of the pulse width). Each then passes into a Philbrick 4855 sample-and-hold circuit with an aperture uncertainty time of 0.25 ns. (This "fast" apertur-ing eliminates the possibility of phase jitter in the subsequent digital samples representing the range-gated signals). From there, the signals are converted to 10-bit binary digital numbers by two Philbrick 4131 analog-to-digital convertors every 10 μs*. The output of the two channels (I & Q) at this point now consists of two streams of 10-bit numbers, which represent samples of the analog signals taken every 10 μs. In order to eliminate
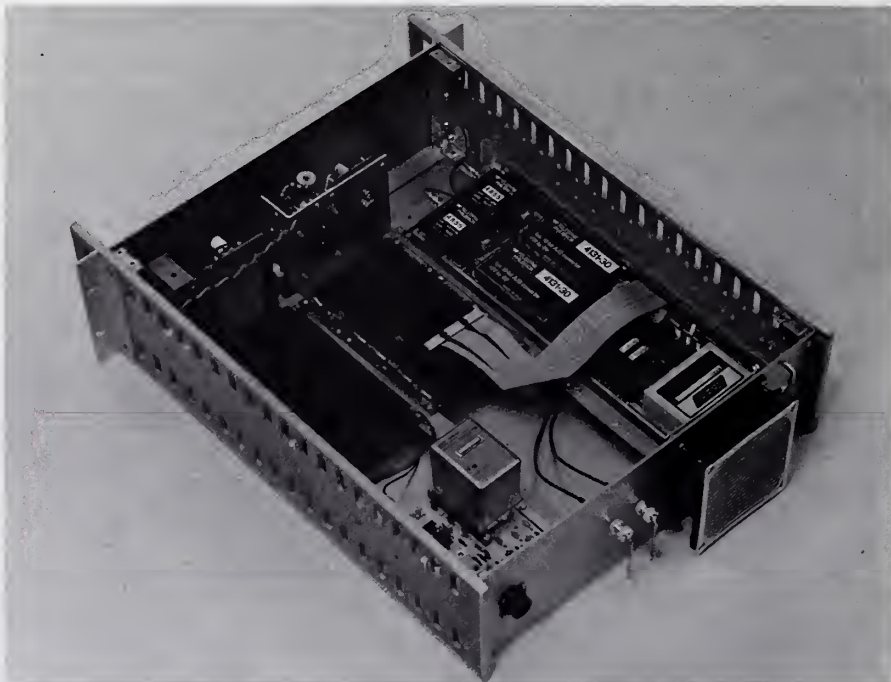
Figure 10. A/D hardware and system timing module.

---

* The receiver signal is actually sampled every 10 μs, even though indepen-dent range gates are obtainable only every 20 μs because of the 20 μs pulse width; subsequently, however, only every other sample word is to be retained for processing.
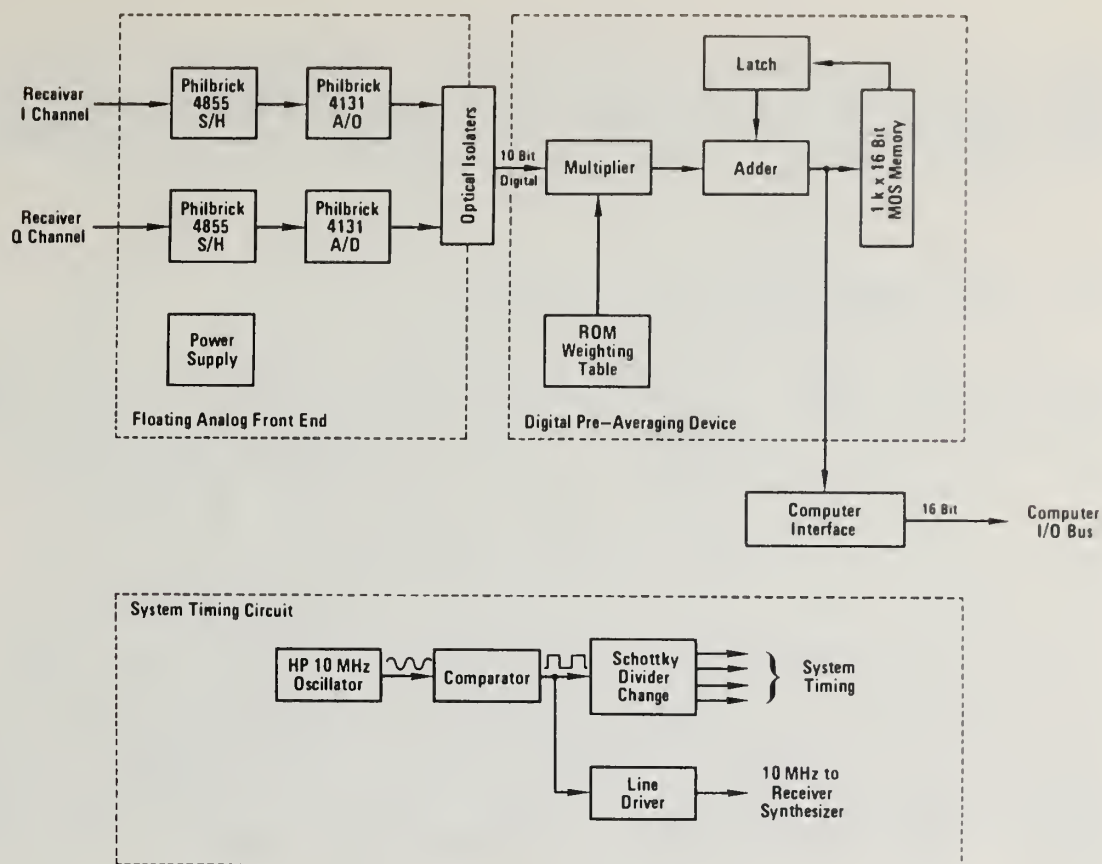
14

Figure 11. Block diagram of A/D hardware and system timing module.

interference caused by ground current loops through the chassis and electronic components, the analog front end of the module is coupled into the digital hardware by means of solid-state optical isolators.

The second function performed within this module is the pre-averaging. This digital operation has the same effect as a filter whose bandwidth is the reciprocal of the pre-averaging time, in this case (nominally) one-half second. To simulate a good filter with a sharp rolloff in the frequency domain, these digital time samples are weighted in a predetermined manner before being averaged. The weighting constants multiplying the digital samples are stored in a read-only memory (ROM). After multiplication, the samples are summed for one-half second by TTL 74181 ALU-chips (arithmetic logic units) and stored in a Type-2102 MOS memory array. The output is then transmitted to the computer I/O bus through a commercial non-processor request (NPR) interface supplied by MDB Systems, Inc. (This interface device is also used in the fast-Fourier transform processor.)

The third function performed in this module is system timing. The heart of this device is a temperature-controlled 10.0 MHz Hewlett-Packard oscillator having a drift less than one part in 10^{11} (within one second). All timing signals (for carrier frequency synthesis, pulse generation,

15

sample-and-hold, computing sequencing, etc.) are obtained by using this signal in combination with digital dividers and combinatorial logic. The basic precision of the oscillator allows measurement of received Doppler shifts to an accuracy of 0.002 Hz at the 30 MHz carrier frequency.

3.1.2 Semiconductor Mass-Storage Module

This unit is shown functionally in Fig. 8. Basically, it accepts and rearranges the output digital data from the A/D Hardware & System Timing Module in a form that can readily be used to fill the input arrays required of the FFT module. It consists of a 32K by 18-bit-word semiconductor memory that is configured (in conjunction with a Linc-Tape digital recorder unit) to operate like a magnetic disk storage device. By storing one-fourth of the data required every 256 seconds for all of the Fourier-transform processing, it will repack this data on magnetic tape in four sets of blocks; hence for each of the three receiving antenna channels and each of the 32 range gates, all 512 words (each) of the I and Q channel data are packed on the digital magnetic tape sequentially. These two sets of 512 words (stored and packed 128 words at a time) represent the real and imaginary parts of the signal time series (each word is one-half second apart in time) that become the input to the FFT. The semiconductor memory cards are manufactured by EMM, Inc., and utilize 4K by 1-bit static memory elements. The module was assembled in-house and is shown in Fig. 12.
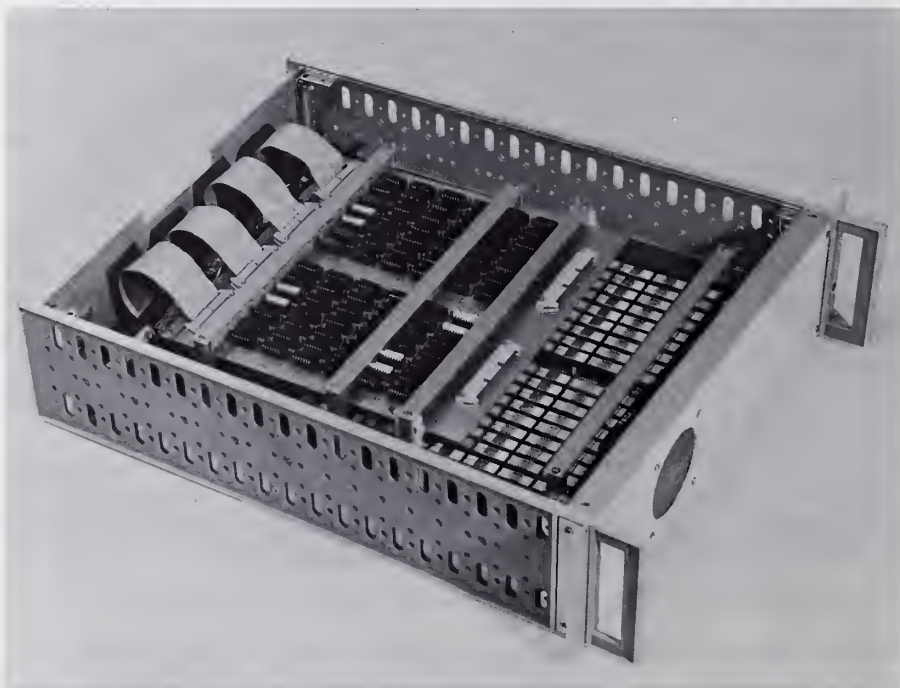
Figure 12.   Semiconductor mass-storage module.

16

3.1.3 Fast-Fourier Transform (FFT) Processor

By designing and constructing this module in house, we have arrived at a unit that is extremely fast at a considerably lower cost than commercially available FFT processors. A block diagram of the unit is shown in Fig. 13. A 512-point (complex) Fourier transform requires approximately 7 ms to complete, excluding input/output time. (This time can be reduced to $\sim$ 3 ms by replacing the present Type-2102 MOS memory in the module with Type-93415 bipolar memory). The speed is made possible by a state-of-the-art two-chip 16-bit binary multiplier. This device, manufactured by AMD, Inc., allows a complex-multiply operation to be performed in $\sim$ 1μs. While only 512-point complex transforms are now currently envisioned, the present module contains sufficient memory storage for a 1024-point complex transform. A photo of the module is shown in Fig. 14.

3.1.4 Linc-Tape Recorder

This storage device from Computer Operations, Inc., (Fig. 15) was selected over alternatives (e.g., "floppy" disk or large 7- or 9-track tape drives) primarily because of its extreme reliability and compactness. (A dual-track redundant phase-recording technique is employed.) The tape is used in conjunction with the Semiconductor Mass-Storage Module (discussed in Section 3.1.2) during system operation. Its principal function, however, is to store the final output surface-current-vector data required to produce a map (after combination with similar data from the other site). The unit stores approximately 147K by 16-bit words of digital data on a 300-foot spool of 1-inch magnetic tape.

3.1.5 PDP 11/04 Minicomputer

The heart of all of the digital signal processing and radar control programming is the PDP 11/04 minicomputer (Fig. 16); it was purchased from the Digital Equipment Corporation, Inc. One is required at each site. The reader is referred to company manuals for a complete description of this device. The computer mainframe contains additional room for other digital devices. Following are the interfaces that are to be inserted into the computer mainframe and extender chassis for use in the current-sensing radar:

   a) 28K words of semiconductor parity memory with battery backup.

   b) Hardware multiply/divide unit.

   c) ROM diagnostic routines.

   d) ROM trig-function lookup tables.

   e) Linc-Tape interface.

   f) Two asynchronous communication interfaces.

   g) A/D Hardware & System Timing Module interface.

17

Figure 13. Block diagram of Fast Fourier Transform processor.
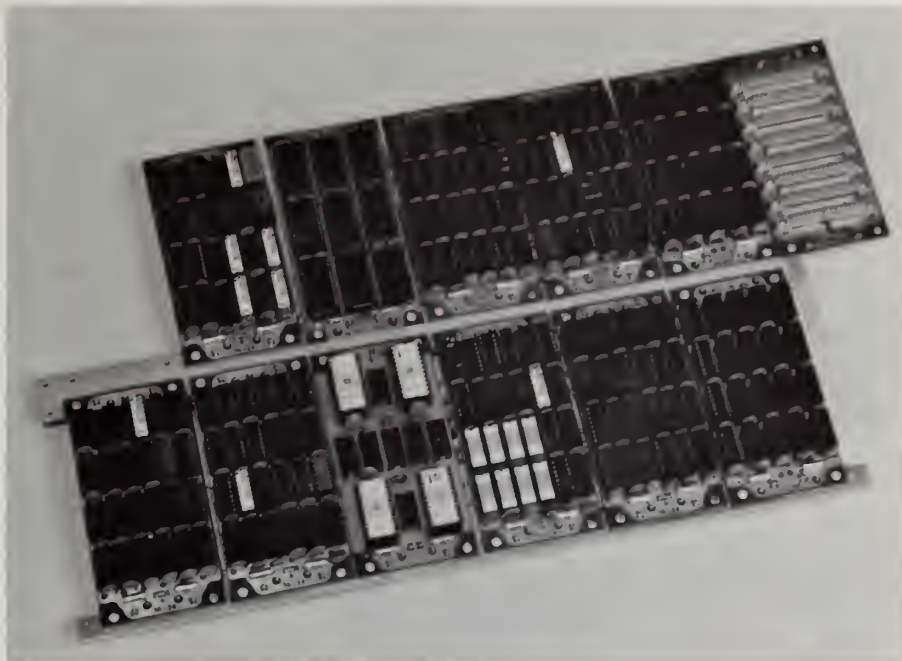
Figure 14.   Fast Fourier Transform module.
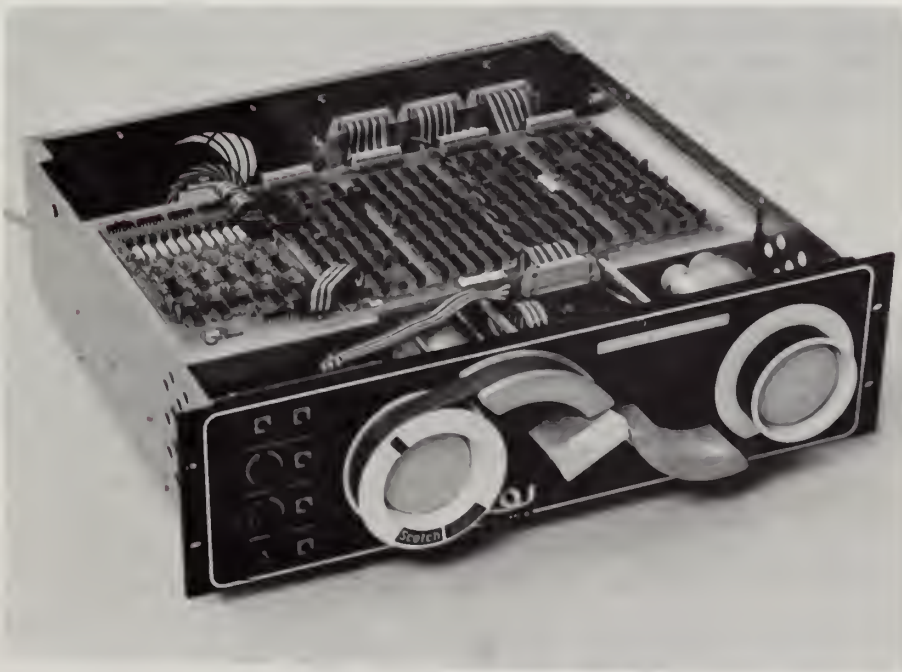
Figure 15.   Linc-Tape recorder.
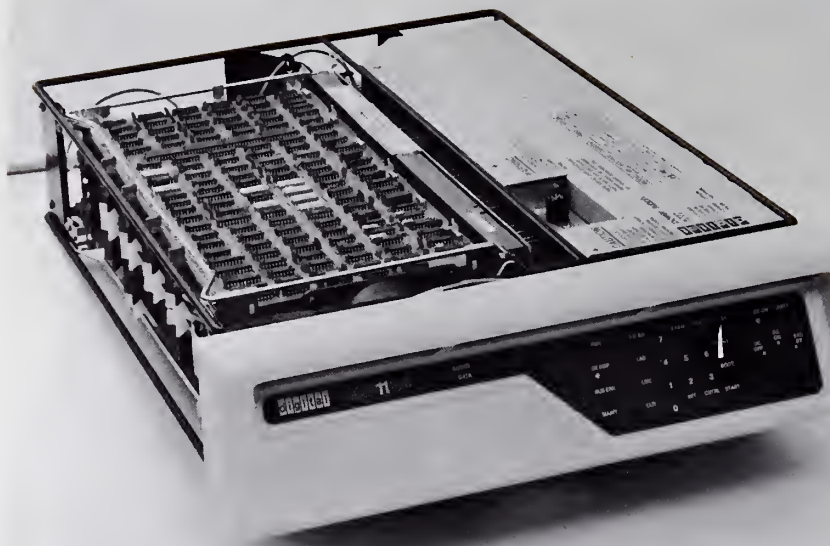
Figure 16. PDP 11/04 minicomputer. (Front panel to be used is from PDP 11/34 minicomputer.)

h) Semiconductor mass-storage interface.

i) FFT processor interface.

j) Receiver interface.

k) Digital plotter interface.

l) Video graphics interface.

m) System status interface.

3.1.6 Keyboard/Printer Terminal

The operator communicates with the radar system entirely through this device. It was purchased from Texas Instruments, Inc., and is their "Silent 700 Terminal" (Model 735, shown in Fig. 17). The terminal operates at a rate of 30 characters per second (300 baud). The printed hard-copy output employs a thermal process to form the characters.

3.1.7 Graphic System

.Plots, curves, and other pictorial data (including the final current map) can be displayed for the operator by this 10-inch Conrac rack-mounted video monitor. The input to this scope monitor comes from a graphic generator manufactured by Intermedia Systems, Inc. The overall system is capable of

20

Figure 17.   Keyboard/printer terminal.

displaying 65K points of data in a 256 x 256 grid on the video scope monitor.
Data from the computer, to be displayed, are stored on the graphic generator
board in a 4K by 16-bit dynamic memory.

A hard-copy map of surface currents (as well as hardcopy of other
desired graphic outputs) is obtained from the Zeta Research digital incre-
mental pen-plotter (Model 130, capable of 300 steps per second).   The
plotter — as well as the video graphic system — is driven by a version of
Calcomp software developed in-house.

3.2   Transmitter

The transmitter system was designed in-house because a suitable device
could not be found commercially; currently available transmitters are both
too large and too expensive. The transmitter chain designed and built here
consists of three submodules (see Fig. 18 for a transmitter block diagram):
(i) the control and power submodule; (ii) a low-level driver amplifier;
(iii) four high-level final amplifiers.

The input to the driver amplifier is a +10-dBm, carrier-frequency, 20 μs
RF pulse from the synthesizer portion of the receiver.   The RF pulse has
been "pre-shaped" in the time domain to effect a bandpass filtering of the
signal, in order to contain the signal energy within specified frequency
limits.   The driver utilizes three stages of broadband (capable of operating
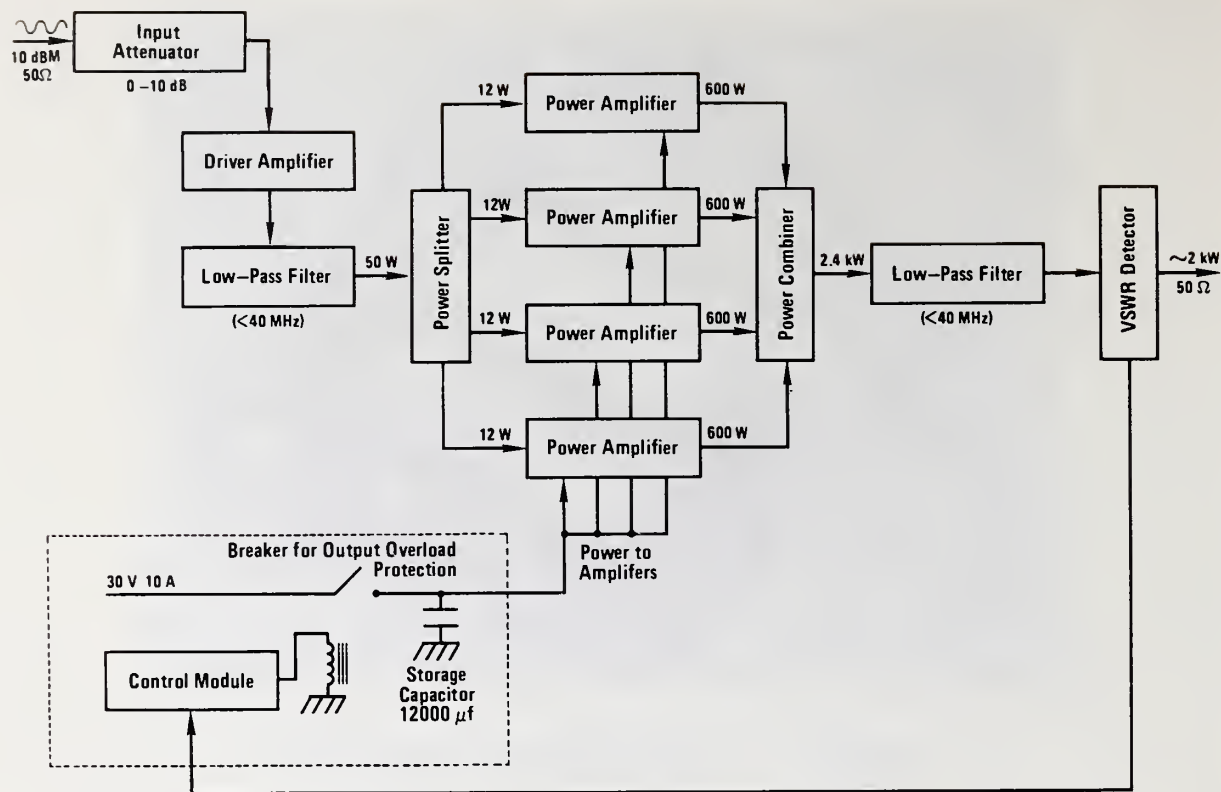
21

Figure 18. Transmitter/Amplifier block diagram.

from 2 to 35 MHz) linear push-pull amplifiers, operated "Class AB". A
photo of the driver unit is shown in Fig. 19.

Output power from the driver is to be a minimum of 50 watts across the
band from 25 to 35 MHz. This driver output is applied to a low-pass filter
with a cutoff of 40 MHz in order to prevent transmission of spurious har-
monic interference (at 2, 3, 4, ... times the carrier frequency). The low-
pass filter output is then coupled to a 4:1 power splitter, which in turn
is connected to the input of each of four final-power amplifiers.

The final amplifiers utilize four TRW PT9780 transistors configured in
two push-pull pairs. A fifth transistor (a TRW PT9780) is used as a tempera-
ture sensor in the AB bias system to prevent thermal runaway. The amplifiers`
employ ferrite-loaded brass tubes as broadband transformers. (The ferrite
loading is required only at the lower frequencies.) The amplifier gain is
∿ 16 dB at a peak-power output level (per final amplifier) of ∿ 600 W from
25 to 30 MHz. This level is obtainable only under the low duty-factor
operation of the present system (i.e., a 20 µs pulse at a 1 kHz pulse-
repetition frequency gives a duty factor of 2%). The positive temperature
coefficient of the PT9780 emitter-ballast resistor causes the power output
to drop as the device temperature rises. The heat sink for these amplifiers
has been designed to handle the normal 2% duty-factor operation, but a
high-level sustained CW output cannot be tolerated. The present unit has

22
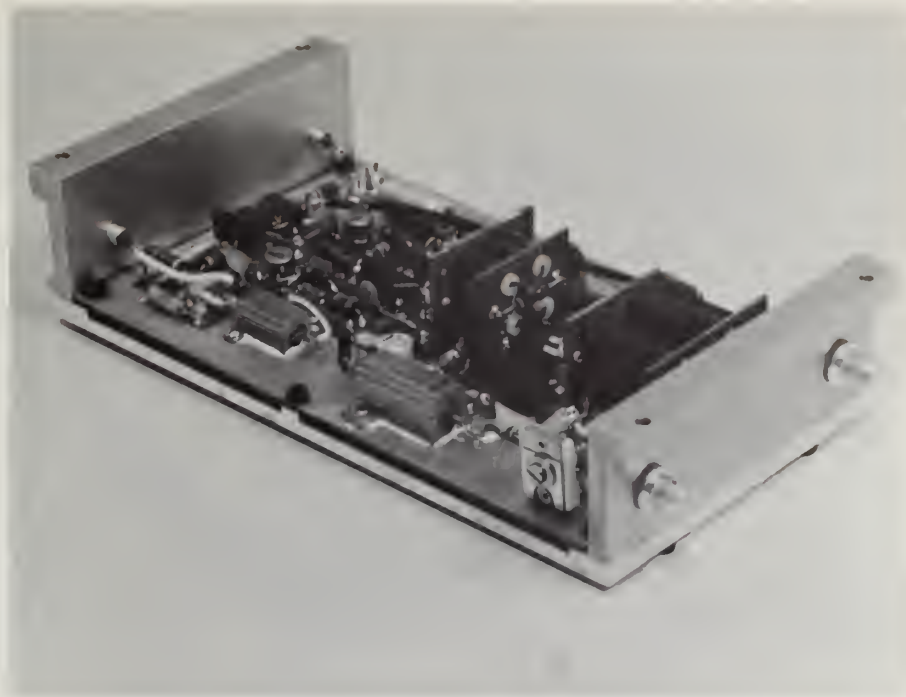
Figure 19.   Prototype transmitter driver-amplifier.

shown no tendency toward instability in laboratory tests, and has shown an ability to survive both open and short circuits on the amplifier output. A photo of the amplifier is shown in Fig. 20.

In order to generate over 2000 W peak power at 30 V (for all four amplifiers), a power supply must be capable of delivering almost 100 amps of current during the pulse duration; a unique power supply was developed for this purpose. This supply operates by charging a special Sprague low-impedance, high-current capacitor from a 30-V, 10-amp switching regulator at a controlled current level. During the 20-µs pulse passage (through the amplifier), the required high current is supplied by discharging the capaci-tor. In the event of a timing failure, in which a CW signal (instead of a pulse) would appear at the amplifier input, the capacitor would simply discharge to a low level to prevent sustained large currents that would produce overheating. Also, if a voltage standing-wave ratio (VSWR) detector at the transmitter output senses the presence of either an open or short circuit across the antenna system, a relay opens so that the capacitor cannot be charged, causing the system to shut down. Either of these fail-ures will cause an error condition message to be sent to the computer, which in turn notifies the operator by means of the system console. Finally, additional circuitry is included to provide a hard "shutdown" of the trans-mitters between pulses in order to prevent amplification and radiation of broadband noise; if unchecked, this can be a problem with linear amplifiers.
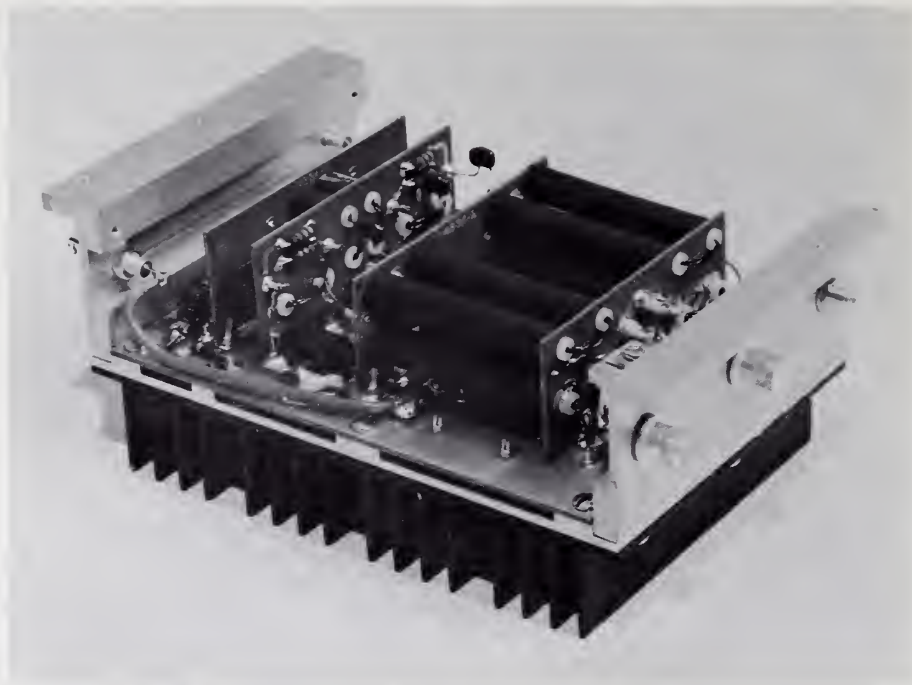
Figure 20.   Final transmitter power-amplifier.

3.3 Receiver

The receiver is by far the most sophisticated RF component in the current-sensing-radar system. For lack of time and experience, we have contracted out the design and construction of this item to Barry Research, Inc. It will be discussed here, therefore, from the standpoint of a functional block diagram and the parameter specifications that the contractor is meeting. Fig. 21 shows the receiver block diagram.

The heart of the receiver is the frequency synthesizer. It generates both the (selected) transmitter carrier frequency, as well as all of the frequencies required for mixing in the receiving process. Let us start first with the transmitted signal. The frequency synthesizer receives a 10 MHz stream of square pulses from the A/D Hardware & System Timing Module. The 10 MHz frequency of this input is divided down to 200 kHz within the synthesizer, so that any frequency between 25 and 35 MHz can be selected in 200 kHz increments. The operator in fact determines the frequency by means of a thumbwheel "channel selector." The CW signal from the synthesizer then passes through a gate, whose duration and timing is also controlled digitally by the A/D Hardware & System Timing Module. This gate forms and shapes the pulse-modulated carrier signal (at a +10 dBm level) which then passes into the transmitter driver.

Part of the CW carrier signal from the synthesizer passes through the calibration box, which square-wave modulates the carrier at a 0.5-Hz rate. The signal is then available at the receiver input for calibration purposes;
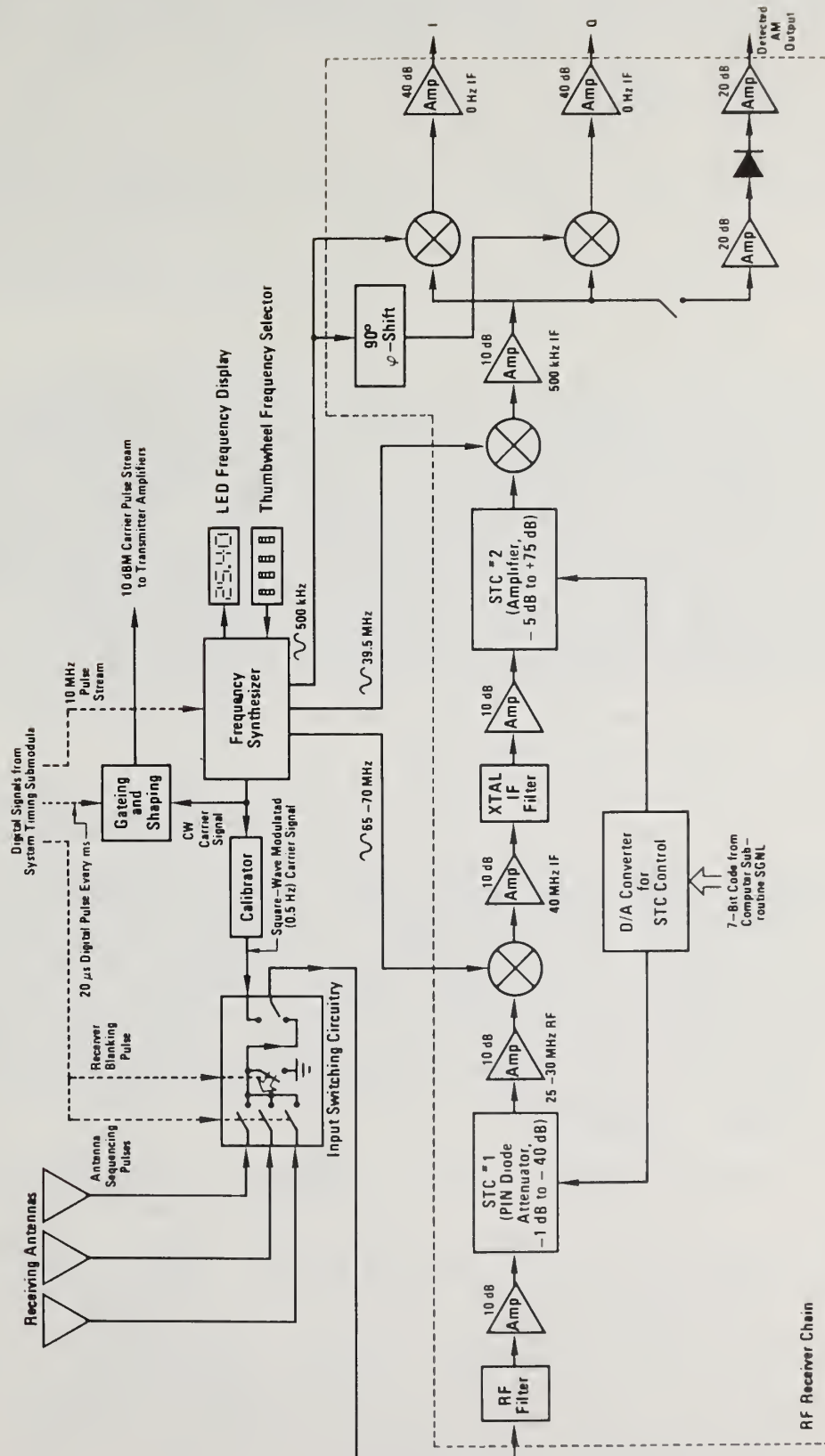
24

Figure 21. Receiver block diagram [designed & constructed by Barry Research, Inc.]

it will emerge from the receiver with energy at the usual 0.5-Hz sidebands of a square-wave signal. The operator can select the power level of this calibrate signal to be either -17 dBm or -57 dBm; these power levels will produce 0.5 Hz sidebands at the output of -37 dBm and -77 dBm, respectively, for reference purposes.

The actual receiving process starts some 20-40 μs after radiation of the transmitted pulse. During transmission, the receiver front end is shorted by a blanking signal (also from the A/D Hardware & System Timing Module) in order to prevent damage from the intense transmitted signal. Then one of the three antennas is switched to the receiver front end by PIN diodes for a duration of ∿ 940 μs; the digital switching signals also come from the same timing submodule.

Because the received sea-echo signal power on the average decreases with range, R, (or time after transmission, T) at a rate greater than R^{-3} (or T^{-3}), the received signal dynamic range will greatly exceed the 60 dB dynamic range of the A/D converter. (The radar receiver has a dynamic range of 100 dB at a 20-dB signal-to-noise ratio.) The usual radar technique employed to make the received signal's large dynamic range compatible with the limited A/D converter dynamic range is to use what is referred to as a sensitivity-time control (STC). This means that the effective receiver gain is switched in pre-programmed steps as a function of time, to remove the signal falloff with time. In our Barry receiver, this is accomplished in two stages. In the first, PIN-diode attenuation steps are switched in, providing attenuation from -1 dB to -40 dB vs. time. The second stage switches in amplification steps, from -5 dB to +75 dB vs. time. The stepping sequence for both of these STC stages originates with a 7-bit binary code originating in the computer; this passes into a digital-to-analog (D/a) convertor which converts the digital signals to attenuation/amplification steps for the two STC stages. The actual attenuation/amplification steps are stored in random-access memory (RAM) buffers of a computer interface, and are transmitted to the D/A convertor as a 7-bit code; the step-change rate (i.e., every 20 μs, corresponding to the pulse/range-gate resolution) originates from the system timing submodule. Before each "map-run" begins, the computer determines the attenuation/amplification steps vs. time by sampling the returns from each of the first 32, 20-μs range gates during a test transmission. The entire STC process allows greater signal dynamic range, thereby allowing maximum signal resolution by the A/D convertors and subsequent FFT processor.

The received frequency at the transmitter and receiver front end will in practice be selected from the region between 25 and 30 MHz (although the receiver is capable of operating between 2 and 35 MHz). Subsequently, the signal is mixed to a fixed IF value of 40 MHz. After the second STC stage, the signal is mixed to a second fixed IF value of 500 kHz; the signal is band-pass limited at 40 MHz with a crystal IF filter bandwidth of 50 kHz, the reciprocal of the pulse width. Finally, two channels at a zero IF frequency value are generated by mixing two 500 kHz reference signals (from the synthesizer) — one shifted by 90° with respect to the other — to form the receiver output I (in-phase) and Q (quadrature) signals required for subsequent complex Fourier transforms.

26

An AM output channel is also provided (50 kHz wide) to allow the operator to switch off the transmitter and "listen" at various possible frequencies to make sure he is selecting a channel free of interference.

The receiver front end has been designed with a noise figure of 10 dB; this is adequate below 30 MHz because the dominant noise is external to the system. The receiver has also been designed to provide "status" signals from various locations within the module to indicate to the operator the integrity of the receiver.

3.4 Antennas

Radar systems that can scan and map the echo return over areas with reasonably good resolution are typically many wavelengths in physical size. At HF, this often involves antenna lengths of hundreds of meters, which in turn requires leasing large amounts of land. Therefore, the antenna for many previous HF radar systems has been the major factor limiting mobility and driving up the cost. The azimuthal mapping techniques discussed previously were selected so that the antenna size and complexity could be reduced. Our antenna systems have dimensions no more than a few meters, and consist of simple elements — resembling the "vertical whip" automobile antenna — which can be erected and dissembled on the beach in a matter of minutes. As it turns out, the antennas are one of the lowest-cost components of the system.

3.4.1 Transmitting Antennas

The transmitting antenna is to be partially directional. Fig. 22 shows a photo of this antenna. It is known as a vertically-polarized Yagi monopole array, and is to consist of three or four vertical elements. Only one vertical element in this type of antenna receives the input power from the transmitter; the others are known as parasitics, and serve to direct the radiated power forward. It is anticipated that the radar system will be allocated approximately six frequencies slightly below 30 MHz by the Interdepartmental Radio Advisory Committee (IRAC); the operator will select the particular frequency for a given operating period at the site, choosing the "cleanest" channel (free from noise and interference). Therefore the transmitting antenna must be capable of being "matched" to the particular frequency selected by the operator.

Matching is a problem at HF that is germane to transmitting antennas only. The ultimate objective of the transmitter portion of the system is to illuminate the desired sea area with the greatest possible power. This is possible only if the radiation resistance of the transmitting antenna is equal to (or matched to) the output resistance of the transmitters and characteristic impedance of the transmission line; in addition, the total reactive portions of the impedance in the antenna and transmission line/ transmitter outputs must cancel. Antennas of the type shown in Fig. 22,

27

Figure 22.   Transmit antenna.

with the advantage of being simple and compact, nonetheless have the dis-
advantage that their input impedance varies with frequency.   Therefore,
although the antenna can be readily designed to be matched at one frequency,
it can be badly mismatched at another operating frequency selected later,
only two or three megahertz away, and hence radiate poorly. Optimal match-
ing can be achieved at a given frequency (while retaining the desired
radiation pattern) by varying the heights of and spacings between the
vertical whips. Thus the mechanical design calls for telescoping whips and
sliding sections of the metallic basebar. It is intended that the antenna
will be precalibrated by tuning it to each of the frequencies allocated by
IRAC. The spacings and whip heights corresponding to the matched condition
at each of these frequencies will then be marked on the sliding elements.
Hence the operator in the field — upon selection of his operating fre-
quency — would slide the various antenna elements to their respective
"matched" positions.

The general Yagi antenna has been used for many years, and much is
known about its performance. It has the desirable properties of maximum
gain (at a given frequency) for minimum size. We need to know the precise
quantitative relationships between the number of elements, their heights,
spacings, and the electrical properties of the nearby ground, as these

affect the radiation pattern, input impedance, and bandwidth of the antenna. To this end, we are having a team at LLL (Lawrence Livermore Laboratories) — leaders in the field of digital antenna design/optimization — do a study of these parameters.

Preliminary results from the LLL study have shown that the input impedance can be designed to be 50 Ω (purely resistive, and hence matched to the transmitter output/transmission line system) by varying the element lengths. For example, at 25 MHz, using one-inch diameter vertical elements, we can construct a three-element Yagi having 50 Ω input resistance with the following dimensions: reflector height = 3.19 meters; driver height = 3.19 meters; director height = 2.57 meters; reflector-driver spacing = 2.70 meters; driver-director spacing = 0.627 meter; the 3 dB beamwidth of such an antenna is. 150°. A four-element Yagi matched to 50 Ω at 25 MHz has the following dimensions: reflector height = 3.19 meters; driver height = 3.19 meters; first director height = 2.57 meters; second director height = 2.57 meters; reflector-driver spacing = 2.70 meters; driver-first director spacing = 0.75 meter; first-second director spacing = 4.624 meters; the 3 dB beamwidth of such an antenna is 88°. At 30 MHz, the 50 Ω input resistance is achieved for the above three and four-element Yagis by merely changing the heights of the vertical elements, but leaving the spacings the same (the beamwidths remain essentially the same also). The input impedances for the above antennas vary less than 1 Ω (about the nominal 50 Ω input) across a band ± 50 kHz about the carrier; since the total signal bandwidth is 50 kHz, the antenna bandwidth will not distort the signal in any significant manner.

The implications of the above on the mechanical design and field utilization are important. Essentially, the only thing that needs to change based upon the selected operating frequency is the element heights; the remainder of the antenna mount is fixed. Thus, elements having different heights would be cut for each operating frequency; the proper set would be screwed into the base upon selection of this frequency. The decision as to whether to use a three or four-element antenna would be made in the field by the operator, depending upon whether the particular coastline geometry would call for a wide or a narrow antenna beam pattern.

Other results of the LLL study concern the configuration of an acceptable ground screen beneath the Yagi array. By plotting the magnitudes and directions of the electrical currents that would be induced in a perfectly conducting earth, ground screen wires can be configured beneath the antenna in the proper directions, especially where the currents are strong. LLL studies show that our several radial wires shown in Fig. 22 in front of the antenna (running into the sea) are important; those behind the antenna are less important, and can either be shortened or eliminated.
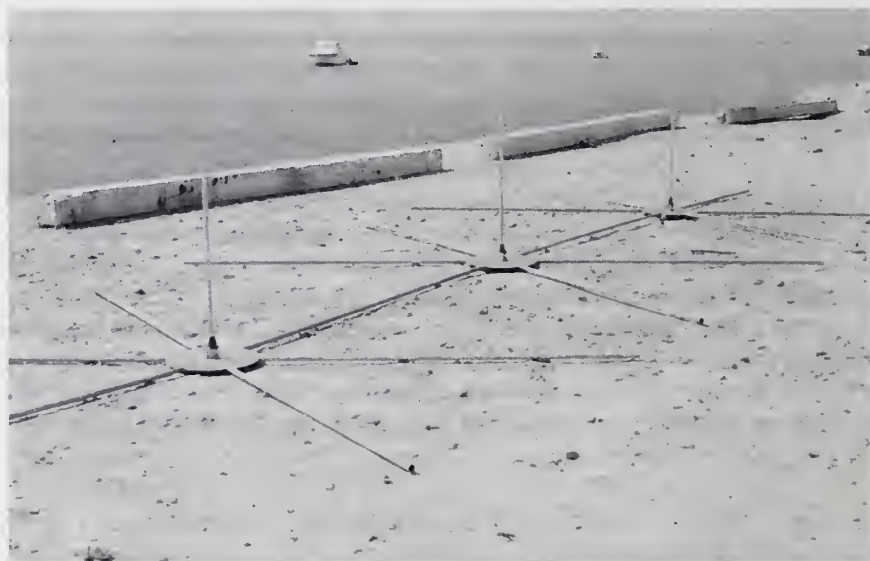
3.4.2 Receiving Antennas

The receiving system consists of three separate antenna elements whose signals are processed and recorded independently. By computing the phase

differences between the signals at the three antennas, the azimuthal direction of arrival is obtained in the digital processing system following the receiver. The mathematics of the present computer software calls for the three antennas to be arranged along a line, with an equidistant spacing no more than one-half wavelength. Fifteen feet between elements, for a total length of 30 feet, is planned. The elements are switched on sequentially, during consecutive pulse transmissions (every millisecond). Hence, each receiving element — acting alone — has an omni-directional (azimuthal) receiving pattern. The receiving antenna system has already been built, and a photograph is shown in Fig. 23. The exact spacing and antenna baseline orientation are parameters entered by the operator during measurements.

There are no stringent criteria for the hardware design involved in an HF receiving antenna, as there are for the transmitting antenna. The effect of a mismatch at the receiving antenna terminals will cause the internal noise (generated at random electron motion) in the receiver front end to increase relative to the externally received signal power. At HF, however, (in contrast to the microwave region), external noise (from atmospheric sources) dominates internal noise typically by 30 dB. Therefore, even if the front-end internal receiver noise were to increase by 20 dB relative to the total externally received signal, the external noise would still dominate internal noise by 10 dB. Hence most HF receiving antenna systems will merely connect the element to (essentially) an infinite impedance receiver front end. This technique is planned for our system also, where the whip elements are to be kept electrically short (e.g., 3 feet) with a high (reactive) intrinsic impedance feeding into a high- impedance receiver input. Such high impedances also have the desirable effect of

Figure 23. Receiving antenna system.

keeping currents on the antenna elements low, minimizing the coupling between receiving elements and also with the nearby transmitting antenna.

4. SYSTEM SOFTWARE

4.1 Radar Signal Generation/Processing Timing

In Section 2.3 we briefly explained the signal and information flow through the system, using the overall block diagram of Fig. 8 to explain the operation of the radar. In this section — as a prelude to discussions of the system software — we describe in detail the sequence of events that occurs within the system during normal radar operation. This sequence of functions must occur automatically and routinely; individual operations in this sequence take place in almost every component of the system (e.g., at the receiving antenna terminals, in the receiver, transmitter, A/D hardware, pre-averaging subsystem, FFT processor, computer, mass storage device). Digital signals from a single system timing unit (specifically, the 10 MHz pulse stream originating in the A/D Hardware & System Timing Module) represent the basic source that controls the timing of all of these events.

The sequence of events is best illustrated schematically by the system timing diagram shown in Fig. 24. The sequence can be assumed to begin at t = 0 when receiving antenna whip #1 is connected to the input of the receiver through a three-way PIN-diode switch. At this time, a 20-μs shaped pulse is provided by the receiver and passes (instantaneously) through the transmitter amplifiers. It is broadcast from the Yagi trans-mitting antenna at ∿ 2 kW power level. During this transmission time, the receiver input is shorted to prevent damage from the intense radiated pulse.

Shortly after t = 40 μs, the receiver is reconnected to the antenna system and begins detecting the echo pulse. At t = 60 μs the two A/D convertors digitize the zero-IF, I and Q channel outputs from the receiver. Thus two "blank" pulse periods are left after the transmitted pulse clears the antennas but before signal processing begins. This process therefore ignores the scatter from a circle around each radar out to 6 km, and hence eliminates echoes from unwanted strong "reflectors" (such as towers or buildings), but results in loss of very little sea current information on the basis of a geographic grid of points every 3 x 3 km.

The sampling and digitizing process continues, with digital samples being weighted and retained in the pre-averaging memory every 20 μs until 32 such samples are collected (at t = 700 μs). Each sample represents the instantaneous echo from one "range gate", with contiguous range gates separated by 3 km. The total range extent from the radar unit permitted by 700 μs delay is ∿ 105 km. (It is not expected that sea echoes will be received above the noise beyond about 70-80 km because of the extreme path loss at greater ranges.) Since both I and Q channel data for 32 range
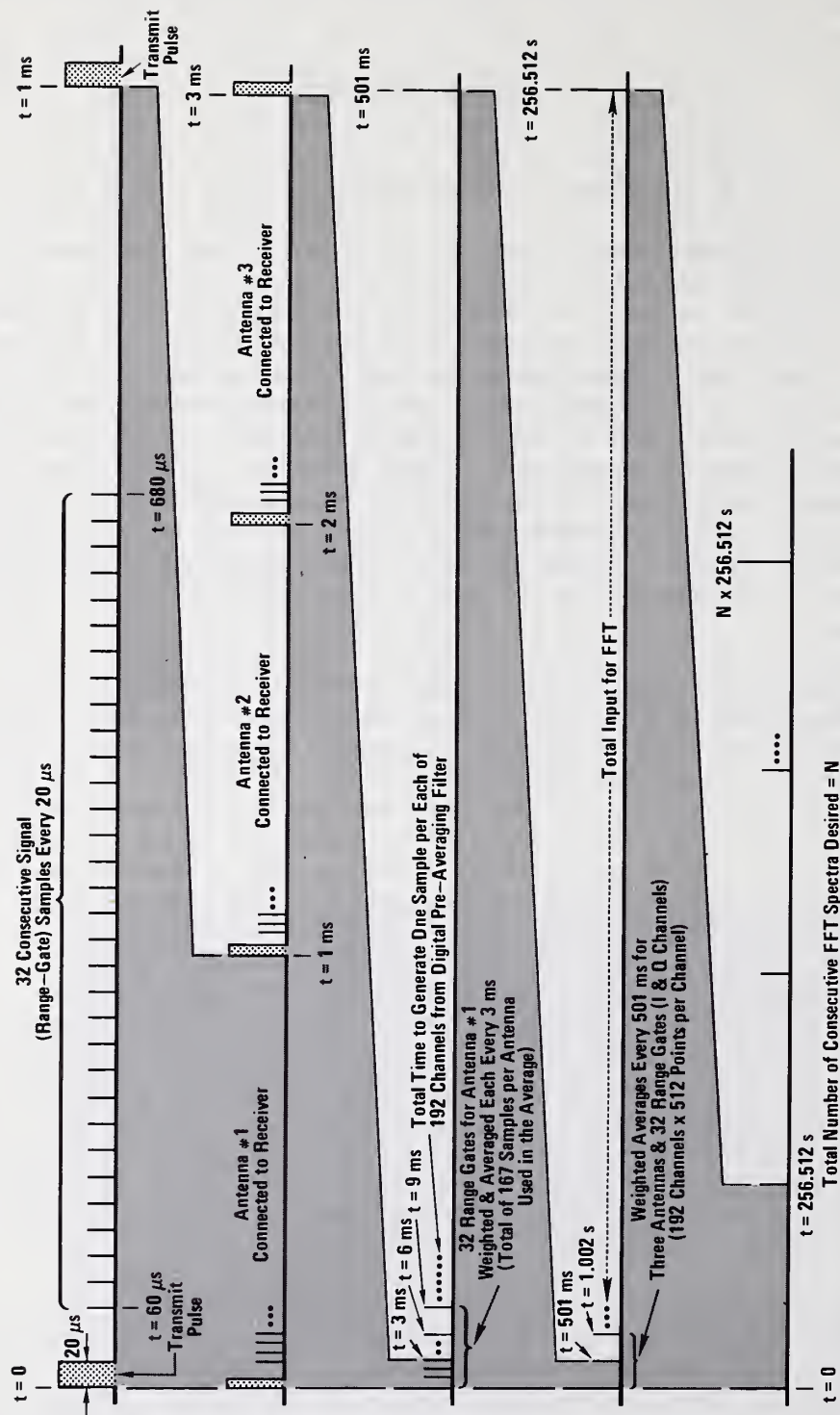
31

Figure 24. System timing diagram.

32

gates are being collected, a total of 64 locations is reserved in the pre-averaging memory for these samples from antenna whip #1 within t < 1 ms.

At t = 1 ms, the above process is repeated (beginning with the transmission of another 20-μs pulse), but now antenna whip #2 is connected to the receiver. These samples are stored in I and Q memory locations 65 through 128 within the pre-averager.

At t = 2 ms, the same process is repeated, but with antenna whip #3 feeding the receiver; the corresponding pre-averaging memory locations reserved for these samples are 129 through 192.

The entire scan sequence switching through the three antennas is now repeated, beginning at t = 3 ms. The resulting 192 samples from t = 3 ms to t = 6 ms are weighted and added to the previous 192 samples stored in the pre-averaging memory. This sequence repeats itself every 3 ms, with running, weighted sums being stored in each of the 192 pre-averaging memory locations. It ceases after one-half second (at t = 501 ms, to be exact); at this point, 167 samples have been collected and added for each range gate and each receiving element to form the 192 weighted sums remaining in the pre-averaging memory. At t = 501 ms, the 192 samples in the pre-averaging memory are transferred through the computer input/output bus to the semiconductor mass storage device. The I and Q channel samples for each of the 32 range gates and for each of the three antennas thus each forms the first complex point in the array of time samples to be Fourier transformed. A total of 96 Fourier transforms are to be taken ultimately (32 range gates times 3 antennas). At t = 501 ms, the process described in the preceding paragraphs repeats itself, terminating at t = 1.002 s, after which time the second complex point of each of the 96 Fourier transform input arrays has been collected. This entire sequence repeats itself every 501 ms, until 512 complex time-series points have been collected as the input for each of the 96 Fourier transform arrays. This collection is completed at t = 256.512 s (after ∿ 4.27 minutes).

At this time (t > 256.512 s), the 96 complex 512-point Fourier transforms are taken sequentially in the FFT processor. Allowing at most 10 ms for one 512-point transform means that all transforms can be completed in ∿ 1 second. Theoretically, a current map can be constructed with one set of such samples (i.e., after only one 256.512-s run of radar operating data). If any portion of the radar signal is random, however (e.g., because of the random amplitude of the sea echo, or the random noise signal, or the random fluctuations in the surface current), it may prove desirable to "average" the results of several such 256-second transforms, to obtain an "average" current map. In this event — which is an option available to the operator — the radar continues with new Fourier-transform cycles being repeated every 256 seconds (4-1/4 minutes) until the operator judges that an adequate data run has been completed, at which point he terminates operation of the system.

Note that no "complete" current vector map is possible until the data from the second site (operating simultaneously but at a second, non-interfering frequency) are combined with the data from the first. The computer processing required for this combination and final map production will most

likely be performed immediately after cessation of the radar operation, although there is no reason this cannot be done during radar operation. In fact a map in fact can be produced as soon as the data from one site can be transmitted (e.g., by telephone or telemetry) to the other.

4.2 Control Software

4.2.1 Interfacing Items Necessary for Understanding of Software

Control software designates the programs (mainly machine language) that permit the operator to interact effectively with and control the operation of the entire current-sensing-radar system. No attempt will be made here to provide a detailed listing of the software; several of the programs have not yet been completed, and some are currently undergoing modification. Rather, the following three subsections will describe the typical functional interactions between the operator and the radar system for which the software is being written. The present subsection discusses the fundamental tools upon which the use of the control software is based.

RSX11S is the designation of the "operating system" (supplied by the Digital Equipment Corporation, the manufacturer of the PDP 11/04 minicomputers to be used in the radar units) selected for use in the field. The operating system is the fundamental software that controls the operations performed by the computer; it permits real-time multi-tasking within the machine. Since there are many tasks to be performed within the computer — both simultaneously and sequentially — the operating system interleaves and schedules these required tasks. The tasks themselves may have been preprogrammed in assembly language, FORTRAN, or Basic. The required portions of RSX11S — along with the control, processing, and display software tasks — are loaded into the PDP 11/04 memory from the Linc-Tape unit before the operator begins a radar run in the field.

The Linc-Tape recorder is used for two other functions during radar operation. After RSX11S and the associated tasks have been loaded into the machine memory, a blank tape reel is placed on the drive. This reel is first employed simultaneously with the radar operation and real-time data processing as a temporary storage medium; in conjunction with the semi-conductor mass-storage device, data are rearranged in array form to be used as the complex input to the FFT processor. Finally, the tape is utilized to store a permanent copy of the current map.

All communication between the operator and the system occurs through the Texas Instruments "Silent 700" terminal and the video display monitor (a cathode ray tube). The former unit not only provides a keyboard from which the operator enters commands, but also gives a permanent hardcopy printed output of these commands and the routine status of the system (similar to a "log"). The video display monitor will display graphic data for the operator, such as sea-echo Doppler spectra and current-map data; if

34

he desires, the operator can obtain a permanent hardcopy of such graphic
output on the Zeta digital plotter.

A MODEM with an acoustic coupler provides digital communication between
the radar sites by way of either a 172-MHz telemetry link or a normal
telephone (where the latter service is available). Thus, map data can be
transferred between sites so that a complete map can be constructed. In
addition, the site operators can communicate with each other (by voice)
using either the radio or telephone.

4.2.2 Prelude

For the sake of discussion, the system control software is divided
into three groups, depending upon when it is being executed. The prelude
group includes those functions performed between man and machine before the
actual radar data-taking begins. Software for these functions is best
described by illustrating the interactions that occur between the field
operator and the system at the keyboard terminal.

First, the operator turns on the system power, the computer, and then
loads RSX11S (and the associated system tasks) from tape into the PDP 11/04
extended memory; he immediately replaces the tape reel with a blank. The
computer then automatically performs diagnostics on itself and on other
system hardware to make sure everything is running as per design; if any
fault occurs, the computer will print out (at the terminal) where the fault
occurred and what happened.

When everything in the system has been automatically checked out, the
computer will query the operator for pertinent processing data. These data
include: (i) time and date; (ii) geographic position (latitude and longitude
of the two sites); (iii) receiving antenna baseline orientation; (iv) radar
frequency selected for operation; (v) relevant meteorological data (such as
wind speed, direction, tidal phase) for later referral and correlation;
(vi) planned length of operation. After completion of this exchange (which
is recorded in hardcopy form as a permanent record), the machine, upon
command from the operator, initiates its first 256-second radar data run.

4.2.3 Interlude

The interlude group of computer functions includes all those that take
place during the operation of the radar (i.e., during transmission and
reception). These tasks may be divided into two categories: foreground and
background processing. Foreground processing includes all of the real-time
data manipulation and mathematics required to obtain the final output
current map; by real-time we mean those tasks that run simultaneously with
radar transmission and reception. Most of the foreground tasks will be
described in the subsequent section on signal-processing software.

Background processing involves "housekeeping" tasks not obviously related to digital radar signal processing. Under RSX11S, various tasks falling under foreground and/or background can be running simultaneously on the PDP 11/04 minicomputers, in a time-share mode. Background tasks will include routine system checks and diagnostics; for example, the transmitter output power level will be monitored, and a message will be printed if it falls below a given threshold. Another check will be made on noise and/or interference; if it exceeds a given threshold, the operator will be notified, at which point he has the option of switching to another frequency. The computer will print routine messages for the operator (without requiring the system to pause), such as one indicating when a given 256-second run is completed.

It is important to emphasize that the evolution of the various interlude tasks and messages will be an ongoing process; as more experience in the field is acquired, it will become obvious what changes can reduce the complexity of the work for the operator and produce a more effective output product. In fact, it will even be possible to program in many functions during operations in the field.

4.2.4 Postlude

At the termination of actual radar operation (whether after one or several 256-second coherent integration periods), an array of digital data stored on the magnetic Linc Tape has been acquired at both stations. Each array contains information regarding the mean component of surface current radial to that station, at a variety of geographic points within the radar coverage area. The information in these arrays may be "raw", i.e., Doppler spectra (including phase) as output from the FFT, or it may have been processed further during the interlude; the actual decision as to how much to pre-process during the interlude has not been finalized. Certainly during the first field tests, very little pre-processing will be done during interlude in order to allow maximum flexibility to examine the data during all phases of the processing. As operation of the system becomes more routine, it is planned that nearly all of this pre-processing be done during interlude, so that a minimum amount of final processing need be done in postlude.

At any rate, a certain amount of data processing must be done at the termination of radar operation before an actual current map is produced. The details of the mathematics behind this data processing will be covered in the next section. Among the functions that may be performed under either interlude or postlude operations include: (i) an averaging of data points; (ii) determination of azimuth angle of arrival (at each Doppler shift); (iii) further averaging of data points; (iv) elimination of points for which the signal-to-noise ratio falls below a predetermined threshold; (iv) interpolation and/or extrapolation for regions where there are no data points; (v) for each range gate, the fitting of a curve where Doppler shift is made a function of azimuth angle-of-arrival; (vi) conversion from Doppler shift vs. range and azimuth (polar coordinates) to Doppler shift vs. x-y

distances to each selected map grid point (rectangular coordinates); (vii) conversion from Doppler shift at each map grid point to radial current velocity at that point; (viii) trigonometric combination of radial current velocities from the two sites to obtain the total current vector at each grid point; (ix) display and/or hardcopy plotting and/or (magnetic) recording of the actual current-vector map, including the coastline and any desired information labels. All of these steps have been run on our PDP computer systems using the software that is to go in the field systems, and the total running time for these processes to the output of the map is expected to take less than ten minutes.

4.3 Signal-Processing Software

4.3.1 Functional Description

The ultimate purpose of the software described here is to convert the received radar signals into a map of current vectors. The processing begins by definition after the completion of the digital FFTs. All digital processing before that is done in real-time by special digital hardware components, as discussed in previous sections. Thus — referring to Fig. 25 — we are excluding from consideration here all of the functions done in the upper left section called RADAR DATA.

Two functional inputs are required to produce a current map: (i) received sea-echo radar data in the form of completed digital FFT arrays, and (ii) geographic data, which are input by the operator. The radar data and their processing will be described here, while the geographic data will be described subsequently. Recall that the radar data for each of the two sites consist of 512-point complex Fourier transforms (i.e., 1024 words per transform) for each of 32 range gates for each of three receiving antennas; such a set of data is collected and available every 256 seconds. In reality, it is expected that only the first 24 range gates will contain adequate sea-echo signal strength to be useable (these gates extend to a range from each site of ∿ 78 km). Hence, processing for purposes of making a map will be conducted only on the data from the first 24 of the 32 range gates*.

Initially, the computer determines the total mean signal power level in each range gate by (complex) squaring and summing all of the 512 output FFT points for each range gate. This value is used to set automatically the receiver gain for that range gate, which we discussed previously as part of the receiver "sensitivity-time control" components. This ensures that full receiver analog and digital processing dynamic ranges are being utilized for the signals from each range gate. The "feedback" manner in

---

* The contents of the 32nd range gate will be used for monitoring purposes as a measure of the noise and/or interference present, since the sea echo at this distance will always be well below the noise.
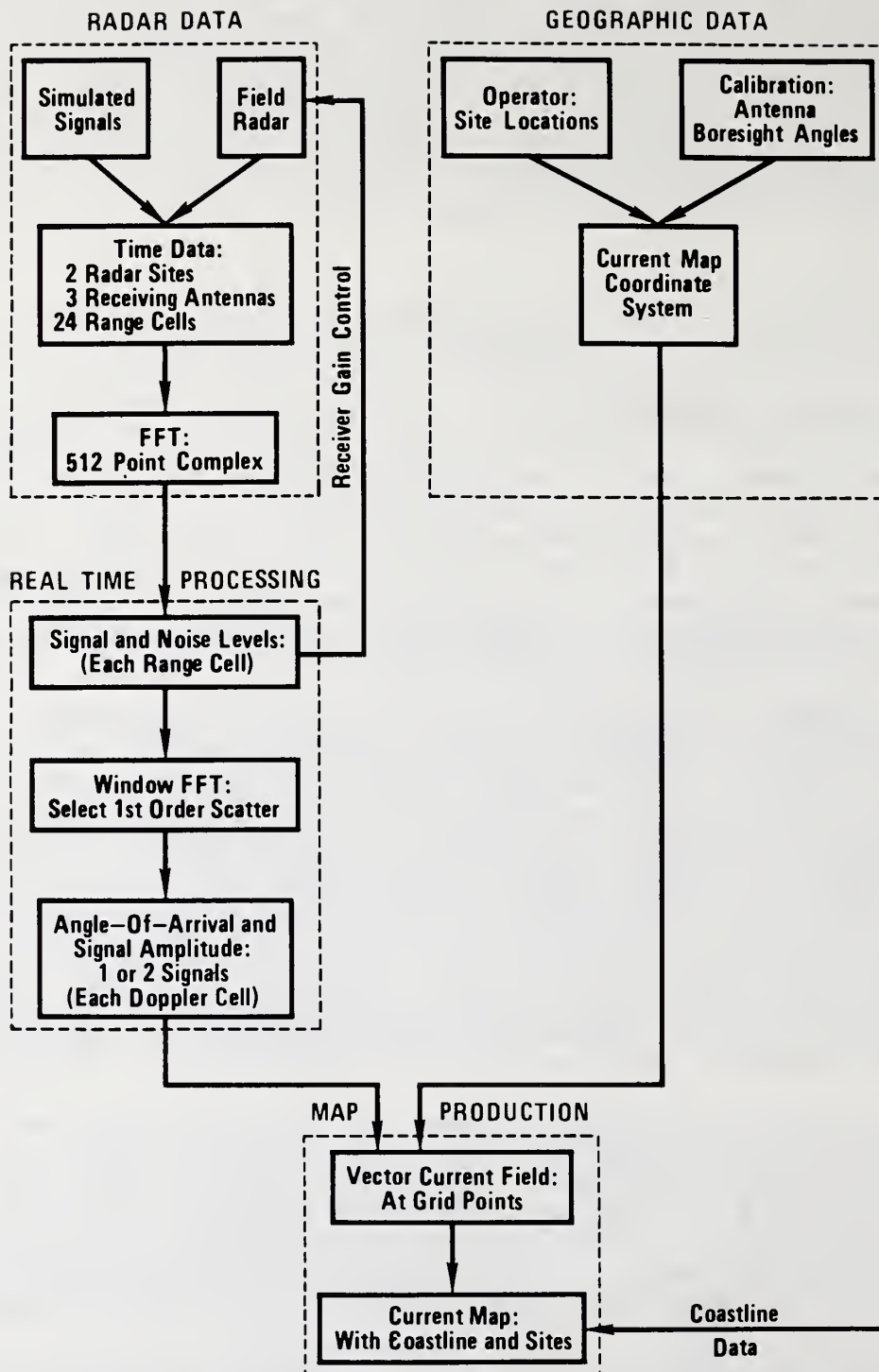
Figure 25. Functional diagram of data processing required to produce a current map.

which the sensitivity-time-control function is performed here is similar to
what is called "automatic gain control" (AGC) in radio receivers.

Next, the spectra (i.e., the sum of the square of the real and imaginary
parts of the FFT at each frequency point) are available for display to the
operator on the video monitor. The operator then (i) selects the stronger
of the two first-order echoes, and (ii) imposes a "window" around the
portion of this echo that he considers to be truly first-order (excluding
second-order regions and/or noise); this he does on the keyboard. He will
probably not do this for all 24 range gates, but only for a few interspersed
across the 24. On the basis of initial experience gained by "operator
windowing" it is planned that ultimately this windowing function will be
done automatically. Therefore, the only data points that will be retained
for subsequent processing are those contained within the window; all others
will be excluded. The width of this window — and hence the number of
points of data retained for processing — is directly proportional to the
radial current shear around the circular range gate. With no current, for
example, the width is infinitesimal and the total number of included points
is only two or three.

Next, the angle-of-arrival of the signals is computed for each Doppler-
frequency included within the window. For the receiving antennas along a
line separated by a distance $\lambda/4$, the angle α is defined with respect to
the perpendicular to the baseline (see Fig. 26). Assuming that (i) the
surface current is not a random variable with time (i.e., for time periods
less than 256 seconds), and that (ii) there is no noise present (i.e., only
the desired first-order sea echo is present), we can obtain the angle, α,
of a signal arriving from only one direction at a given Doppler frequency
uniquely and deterministically using two antennas. Likewise, the angles
α_1 and α_2 of two signals arriving at the same frequency from different
directions can be uniquely determined with three antennas. The relation-
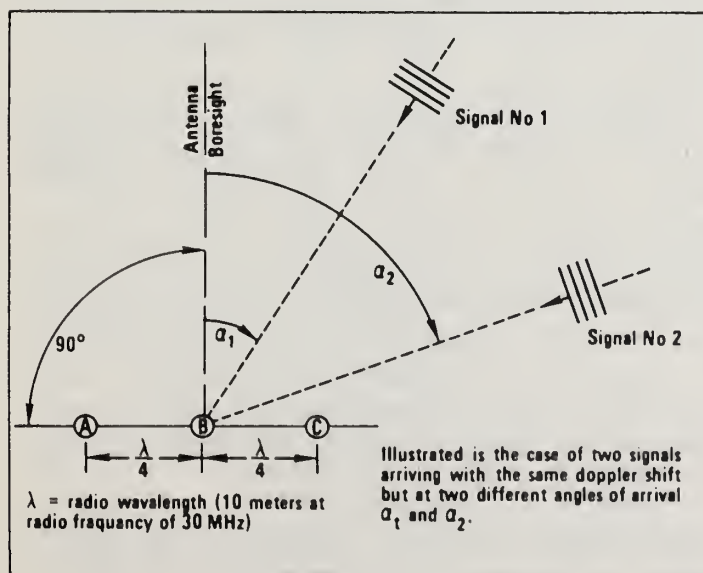ship used to obtain these angles is:

Figure 26. Diagram of three-
antenna resolution of signals
arriving from two directions.

39

$$\alpha_{1,2} = \sin^{-1} \left[\frac{-\tan^{-1}\left(\frac{\text{Im}(x_{1,2})}{\text{Re}(x_{1,2})}\right)}{\frac{\pi}{2}} \right], \tag{1}$$

where $x_{1,2}$ are defined in terms of the complex Fourier transforms of the signals V_A, V_B, V_C at antennas A, B, and C (for a given Doppler frequency) as

$$x_{1,2} = \frac{(|V_C|^2 - |V_A|^2) \pm i \sqrt{4|V_C V_B^* - V_B V_A^*|^2 - (|V_C|^2 - |V_A|^2)^2}}{2(V_C^* V_B - V_B^* V_A)}. \tag{2}$$

The amplitude of the signals arriving from the two directions is given by

$$A_{1,2} = \frac{V_A x_{2,1} - V_B}{(x_{2,1} - x_{1,2})}. \tag{3}$$

This system can handle the situation of only one signal arriving from a single direction α (i.e., $\alpha_1 = \alpha_2$). It cannot resolve signals arriving from three (or more) directions at the same Doppler frequency; it can recognize this situation, however, and eliminate the data point. In practice, it is unlikely that current patterns occurring in nature will produce more than a double-valued ambiguity. Therefore it was decided that the three-antenna system (and related software) would be used unless field experience shows that more are needed.

Furthermore, when noise (or second-order sea echo, which is considered noise for our purposes) is included in V_A, V_B, and V_C, the angles α_1 and α_2 determined in the above manner will not define exactly the direction-of-arrival of the desired first-order signal. In other words, there will be some error, $\Delta\alpha_1$ and $\Delta\alpha_2$, between the true directions and those defined from Eqs. (1) and (2). The error will depend upon the signal-to-noise ratio; the higher the signal-to-noise ratio, the smaller the errors $\Delta\alpha_1$ and $\Delta\alpha_2$. The fact that low signal-to-noise ratios will produce greater errors can be used to eliminate such points; one merely computes A_1^2 and A_2^2, and compares them with a predefined noise threshold to decide whether to retain these points.

Averaging is also used to help smooth the data. Various types of averaging are presently being tested in software simulations. One type will be described here. Assume that there are data points from several

40

256-second FFT runs. For each value of Doppler frequency, Δf_j, that is retained within the window, there will be several values of azimuth angle estimates, $\alpha_i(\Delta f_j)$. We could treat Δf_j as the independent variable, averaging over α for a given Δf_j, or we could treat α as the independent variable, averaging over Δf. We have chosen the latter. We divide the azimuthal sector over which surface currents are sought (e.g., $-90° < \alpha < 90°$) into specified increments, $\Delta\alpha$. Then we average all of the Doppler frequency points falling within the n-th azimuthal bin, $n\Delta\alpha$, as

$$\overline{\Delta f}(n\Delta\alpha) = \frac{1}{M} \sum_{\ell=1}^{M} \Delta f(n\Delta\alpha),$$

where M is the total number of Doppler frequency points in that bin. In certain situations, there may be no frequency points to average in a given azimuth bin; this must be noted for subsequent processing. Thus we arrive at an array of averaged Doppler frequencies vs. azimuth angle, i.e., $\overline{\Delta f}(\alpha_n)$, where $\alpha_n = n\Delta\alpha$. An interpolating curve is now fitted to these points so that Doppler frequency can be estimated at any desired value of α. Among the interpolating curves being tried are a spline fit, a linear interpolation, and least-squares fits; the latter method at present appears to be working the best.

The final process that must be done at each site preparatory to the map graphics is to convert the Doppler shift vs. polar coordinates (i.e., vs. range gate and azimuth angle) to Doppler shift vs. the rectangular coordinates at each selected map grid point. With a map grid specified, the x-y distances from each site are converted to R, α; by interpolation, the Doppler shift at that grid point is determined. Finally, the Doppler shift at that point is converted to a current velocity radial to the given site by using the equation $V_{cr}(x,y) = \frac{\lambda}{2} [f_B - \Delta f(x,y)]$, where f_B is the first-order Bragg frequency and λ is the radar wavelength.

When the data points from both sites are available, the two sets of radial current velocities at each grid point are combined trigonometrically to obtain the total current vector at each grid point (i.e., length and direction). These vectors are available for storage on magnetic tape (for subsequent analyses) or for graphic display on the video monitor and/or hardcopy digital plotter.

In order to establish the angles at each grid point with respect to the two sites (required for the trigonometric vector combination), geographic input data are required as shown in Fig. 24. It is planned that these will be entered by the operators at both sites. The latitude and longitude at each site will be determined by locating the site on a local topographic map. Positional accuracies need not exceed one-half kilometer. Finally, the boresight angle of the linear receiving antenna array must be determined and entered at each site by the operators. This can be done either with a compass or by using transmitted signals from the other site and measuring the phase differences at the separate antennas; both methods will be tried initially in the field.

41

We intend to show a contour of the coastline on the current-vector map. This will help the user to orient himself and also to assess on the spot the practical impact of a current-borne spill on the beach. At present, we have coastline data from the entire continental U.S.A. and Alaska; these data are stored as latitude-longitude points on magnetic tape. It is anticipated that smaller digital tape subsets containing portions of the coastline near our planned operating areas will be prepared ahead of time in the laboratory so that they can be readily used in the field.

4.3.2 Software Description

The preceding section described functionally the mathematical steps necessary to convert the digital radar signals at the output of the FFT into current vectors. This section describes in greater detail the actual computer programs and subroutines for accomplishing this. Not all of the programs correspond one-to-one with the functional blocks of Fig. 25; hence we show in Fig. 27 the actual computer software used for these tasks. All of this software currently exists and has been checked out in FORTRAN against simulated current-modulated sea-echo signals.
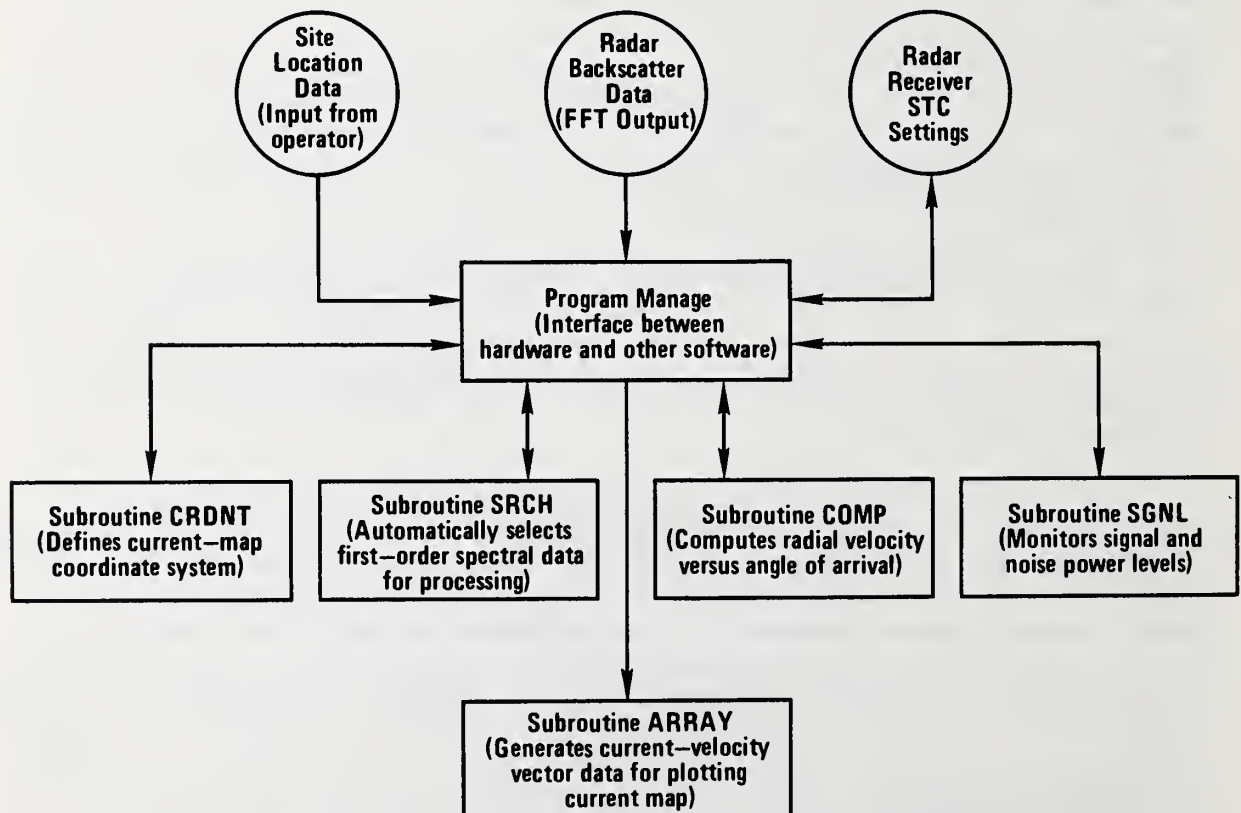
Figure 27. Current-sensing-radar data-processing software.

42

Three types of data are shown here as inputs required for the data processing: (i) site location data, (ii) radar sea-echo backscatter data, and (iii) receiver gain-control data. The site location data consist of the latitudes and longitudes of both radar sites and the angular orientations of the linear receiving antenna arrays at both sites. As described in the preceding section, topographic maps will be used to determine the site locations; most likely, one-way transmissions between the two sites will be used to establish the receiving antenna angles. The radar sea-echo backscatter data consist of the complex array of signal vs. (Doppler) frequency for each range gate and each antenna, as output by the hardware FFT device. These radar backscatter data can either originate from actual signals received in the field or simulated signals; the latter are presently being used in the laboratory to check out the software. Finally, gain-control information is provided for each range gate (i.e., the attenuations and/or gains set in the receiver STC) so that the quality of the data can be ascertained.

The main program MANAGE interfaces the computer hardware with the remaining software subroutines as to the manipulation and processing of the input data; it routes the various data to the proper subroutines for each processing step. Site location data are used within subroutine CRDNT to establish the coordinate system grid for the current map.

Subroutine SRCH automatically determines what portion of a spectrum (FFT output power vs. Doppler frequency) will be retained as the first-order echo. It performs this "automatic windowing" by searching for the higher of the two maxima, and then including everything lying above a preset threshold so many decibels below this peak. A "manual override" will of course be available so that the operator — as he views the spectra on the video display — can set the window and threshold to the position he judges to be optimum. Undoubtedly during most of the initial field operations, human decision processes will be used in lieu of automatic decisions; as more experience is accrued and operation becomes more routine, more and more of these decisions will be made automatically.

After windowing by subroutine SRCH, the data points retained are processed by subroutine COMP. This routine computes the angle-of-arrival of the signal at each Doppler frequency, performs averaging and curve fitting to these Doppler frequency-vs-azimuth points, converts Doppler frequency to radial current velocity, and finally computes the radial current velocity at each of the preselected x-y map grid points. Finally, this information is passed along to subroutine ARRAY — along with similar data from the other site — where a total current-velocity vector is computed at each map grid point by a trigonometric combination of the radial currents from the two sites.

Subroutine SGNL is designed to monitor the received sea-echo signal-power level (i.e., the summation of total power at each FFT frequency) for each range gate so that the gain setting for the receiver STC system can be automatically programmed. One range gate (in which the transmitter signal echo is absent) is reserved for measuring noise and interference power in this same fashion; this information is necessary (i) for operating fre-

43

quency selection, (ii) for continued operator monitoring, and (iii) for ascertaining the mean signal-to-noise ratio for purposes of retaining only meaningful data points.

5.   SYSTEM ANALYSES AND SIMULATION STUDIES

5.1   Signal-to-Noise Ratio (S/N)

5.1.1   Basic Radar Performance Criterion

The signal-to-noise ratio (S/N) is the basic measure of radar perfor-mance. It indicates not only whether the desired signal is likely to be seen above the noise (the detection problem), but also how closely the parameters of the desired signal can be determined as a result of the noise degradation (the precision/accuracy problem). It is obvious that S/N must be greater than unity in order for one to see and identify the desired echo signal.   Noise is always a randomly varying quantity; hence it makes sense to talk only about the average noise power at the output of the receiver. The desired echo signal may or may not vary randomly over time, depending upon the nature of the target. An HF ship echo, for example, is likely to be non-fluctuating. First-order sea echo, on the other hand, is very definitely a random variable [see Barrick and Snider, 1977] whose (voltage) signal fluctuations are Gaussian in nature and which is uncorrelated with itself for consecutive observation times longer than about 25 seconds. When the signal is a random variable independent of the noise, S/N is normally defined by averaging the signal echo power independently from the noise echo power.

Noise at HF originates from external sources. Handbooks [CCIR-322, 1964] of noise have been prepared from extensive, world-wide seasonal/diurnal measurements made in the 1940's and 1950's. Such a noise-voltage signal is a random variable which is spectrally flat over bandwidths less than 100 kHz. This means that if one were to look at the average spectrum of noise (the output of a receiver FFT, squared and averaged), one would observe a constant value as a function of spectral frequency. This constant is defined as N_o^* (watts per Hertz bandwidth, or joules). At 30 MHz, CCIR tables show that total average noise power spectral density referred to the receiver input is:

$$N_o^* = [kT]_{dB} + F_{AM} \qquad \text{(in decibels),} \qquad (4)$$

where kT is the internal noise in the front end of the receiver (at room temperature, T $\simeq$ 300 K, k = Boltzmann's constant = 1.38 x 10^{-23}, and hence $[kT]_{dB} \simeq$ -204 dBJ). F_{AM} is the median atmospheric noise factor. At 30 MHz, this quantity typically originates from man-made noise; at a reasonably

44

quiet location, F_{AM} is 20 dB, meaning that external noise is two orders of magnitude higher than kT (i.e., the theoretically lowest possible internal noise at room temperature). This means $N_o^* \simeq 184$ dBJ.

Let us first assume that the desired signal is originating from a target moving at a uniform velocity*. This target echo will — after spectral processing in the receiver — appear as a discrete spike at a Doppler frequency proportional to its velocity. The height of the echo peak and the reciprocal of its width will then vary in direct proportion to the coherent spectral processing (or observation) time, T_I. One can then define S/N as the height of this signal peak compared with the averaged, flat noise level across the same spectral band. Standard radar textbooks [e.g., Cook and Bernfeld, 1967] show that the best one can do with matched receiver conditions in terms of S/N for this case is given by**

$$S/N = \frac{P_R T_I}{N_o} \, ,$$

(5)

where P_R is the average power available at the receiver front end. The standard radar range equation [Barrick, 1972a,b; Skolnik, 1962] in turn relate the received power to the transmitted peak power P_{PT}, antenna gains G_T, G_R, range to the target R, and radar cross section, σ, of the target as follows

$$S/N = \frac{P_{PT} \, \tau T_I}{T_r N_o} \cdot \frac{G_T G_R F^4}{(4\pi)^3 R^4} \cdot \sigma \, ,$$

(6)

where F is the voltage path-loss attenuation factor; if the path were free space, F = 1. In general for surface-wave propagation beyond the horizon (as in our system above the sea) $F \simeq 1$ at short ranges (less than 10 km), but decreases — eventually exponentially — with increasing range. Barrick [1971] has provided extensive calculations of this factor vs. frequency, range, and sea state; these in turn have been verified by measurements and will be used for subsequent calculations here. The quantities τ and T_r are pulse width and the pulse-repetition interval (as seen at each of the receiving antennas). Since the three receiving antennas are operated sequentially, T_r is three times as long as it would have been had there been only one receiving antenna (i.e., $T_r = 3 \times 1$ ms = 3 ms).

_____

* The actual situation where the received signal is due to first-order sea echo is only slightly different, and will be considered subsequently.

** Since two-sided Doppler processing (i.e., including negative frequencies) is to be employed here, we henceforth use a two-sided definition of average noise spectral density, defined as $N_o = N_o^*/2$.

5.1.2 Sampled Data and Digital Signal Processing

Equation (6) gives a general guideline as to the <u>best</u> signal-to-noise ratio one can hope to realize with any receiver/processor system. It is therefore incumbent upon us to show that the system which we have designed — consisting of both analog and digital circuitry — does in fact achieve this optimum S/N; anything which falls considerably short of this target indicates that our design is inefficient.

Let us start at the output of the sample-and-hold (S/H) and analog-to-digital convertor (A/D) circuits, as shown in Fig. 8. The receiver has an IF bandwidth that is the reciprocal of the pulse width, i.e., $B_R \simeq 1/\tau$. (Here $\tau = 20$ μsec; hence $B_R \simeq 50$ kHz). Within each pulse at the receiver I and Q channel output, the zero-IF (baseband) sea-echo voltage signals (assumed at present to occur at a single frequency, ω_s) are given as

$$v_{SI}(t) = A \cos(\omega_s t + \phi) \qquad ; \qquad v_{SQ}(t) = A \sin(\omega_s t + \phi). \qquad (7)$$

Note that the intrinsic Doppler frequency $\omega_s/2\pi$ of the first-order sea echo is ~ 0.56 Hz at 30 MHz, even though the actual pulsed signal through the receiver has a bandwidth of $1/\tau \simeq 50$ kHz. The sampling gate has a sampling uncertainty time $\simeq 0.25$ ns, so that for range gate j, we obtain a series of discrete values from the A/D convertor of

$$v_{SI}^j(nT_r) = A_1^j \cos(\omega_s nT_r + \phi_1) \qquad ; \qquad v_{SQ}^j(nT_r) = A_1^j \sin(\omega_s nT_r + \phi_1), \qquad (8)$$

where T_r is the pulse repetition frequency per antenna channel (here, $T_r = 3$ ms), and A_1^j is related to A by a constant, K_1.

Select a time t_ℓ at the input of the pre-averager. (The pre-averaging time T_A is fixed here at one-half second.) Therefore, $M = T_A/T_r (=166 \frac{2}{3} \simeq 167)$ values are to be added to obtain*

$$\bar{v}_{SI}^j(t_\ell) = \sum_{-(M-1)/2}^{(M-1)/2} v_{SI}^j(t_\ell - nT_r) \simeq M v_{SI}^j(t_\ell) = M A_1^j \cos(\omega_s t_\ell + \phi_1), \qquad (9a)$$

and

$$\bar{v}_{SQ}^j(t_\ell) = \sum_{-(M-1)/2}^{(M-1)/2} v_{SQ}^j(t_\ell - nT_r) \simeq M v_{SQ}^j(t_\ell) = M A_1^j \sin(\omega_s t + \phi_1); \qquad (9b)$$

---

* In reality, we weight the M values in the summations to improve the filtering quality. The unweighted sums — which we employ here for convenience in the mathematics — give rise to the familiar but rather undesirable (sin x)/x frequency response.

the simplification of these summations is possible because the signal, varying at a 0.56 Hz rate, does not change appreciably in the one-half second averaging time. Therefore, the term inside the summation can be treated as a constant evaluated at time t_ℓ midway during the averaging process. The pre-averager essentially performs the function of a filter with a 1-Hz bandwidth; since the intrinsic sea-echo signal bandwidth lies well inside this width (i.e., 0.56 Hz at 30-MHz operation), its sampled values pass through undisturbed.

Every half-second, a new set of I and Q values is obtained from the pre-averager. Thus, let us equate t_ℓ to ℓT_A, a set of times spaced T_A (one-half second) apart. These values, $\bar{v}^j_{SI}(\ell T_A)$ and $\bar{v}^j_{SQ}(\ell T_A)$, become the real and imaginary part of the input digital FFT array; as they are accumulated, they are stored in the mass-storage device until the specified number is obtained. For the baseline mode of our system, this number is 512; thus the total time required to accumulate this FFT input array (the "coherent integration time") is $T_I = 512 \times T_A \simeq 256$ seconds. After each 256-second interval the FFT processor transforms 32 range gate x 3 antenna = 96 arrays of data; this is done well within the 256 seconds before the collection of the next set of FFT data is completed.

The formal Fourier transform integral of Eqs. (9) can be taken; with no weighting function, it becomes

$$v^j_S(\omega) = \int_{-T_I/2}^{T_t/2} [\bar{v}^j_{SI}(t_\ell) + i\bar{v}^j_{SQ}(t_\ell)]e^{-i\omega t_\ell}dt_\ell , \quad \text{or}$$

(10)

$$v^j_S(\omega) = MT_I A_1 e^{i\phi_1} \frac{\sin(\omega-\omega_s)T_I/2}{(\omega-\omega_s)T_I/2}$$

The actual digital FFT processor approximates the Fourier integral transform by a Fourier series. Thus the output, rather than being a continuous function of ω, is an array corresponding to discrete frequency values $\omega = M\omega_I = 2\pi M/T_I$; for the parameters selected for our system, therefore, the frequency resolution (or distance between adjacent frequency points) is $f_I = 1/T_I = 1/256 = 0.0039$ Hz. The output array lies spaced over a frequency window extending from -1.0 Hertz to +1.0 Hertz. The use of inphase and quadrature data to fill both the real and imaginary parts of the input FFT array allows us to define a non-ambiguous transform over both positive and negative frequency values, a result not possible had we used only inphase (real) values at the FFT input. Note that for a large transform with considerable resolution, the peak value (from Eq. 10) occurs at

$\omega_P = M_P\omega_I \simeq \omega_s$, at which point the peak signal amplitude (from the FFT) is $|v_s^j(\omega_p)| = MT_I A_1$.

Before examining the processing of noise by our system, let us relate the signal amplitude to the received power. Since the average received power was denoted as P_R the peak received power (per pulse) has the value $P_{PR} = \frac{T_r}{\tau} P_R$. We assigned the voltage signal level at the I and Q receiver output channels as amplitude A. The voltage signal at the receiver input can be written $v_S(t) = \sqrt{2P_{PR}R_i}\ \cos(\omega_s t + \phi_I)$, where we note that the received power per pulse is thus merely the amplitude of v_S squared and divided by twice the input resistance, R_i. If we assume a constant receiver voltage amplification gain K_R, then $A = K_R\ \sqrt{2P_{PR}R_i} = K_R\ \sqrt{2R_i P_R T_r/\tau}$, or

$$A_1^j = K_1 K_R\ \sqrt{2R_i P_R T_r/\tau}\ .$$

Let us now examine the noise at the I and Q output channels of the receiver. Since all signals — including noise — have been filtered upon passage through the receiver (with an IF bandwidth $B_R \simeq 1/\tau = 50$ kHz), the signal at the first IF offset of 40 MHz can be considered a narrow-band Gaussian process; hence let us write the baseband IF at the receiver output as

$$v_{NI}(t) = A_N(t)\ \cos\phi_N(t) \qquad ; \qquad v_{NQ}(t) = A_N(t)\ \sin\phi_N(t). \qquad (11)$$

As before, we can relate A_N to the average effective noise power at the receiver input; the latter is $N_o B_R$. Hence, using our previous notation,

$$\langle A_N^2\rangle = 2\langle v_{NI}^2\rangle = 2\langle v_{NQ}^2\rangle = K_R^2 2R_i N_o B_R = K_R^2 2R_i N_o/\tau.$$

In a fashion similar to Eqs. (9), we obtain the following expression for the digital output of the pre-averaging circuit:

$$\bar{v}_{NI}^j(t_\ell) = \sum_{-(M-1)/2}^{(M-1)/2} v_{NI}(t_\ell - nT_r) \qquad ; \qquad \bar{v}_{NQ}^j(t_\ell) = \sum_{-(M-1)/2}^{(M-1)/2} v_{NQ}(t_\ell - nT_r); \qquad (12)$$

here, the bar over the voltages denotes the sample sum of M numbers; hence this sample sum is still a random variable. We can relate it to a noise correlation function defined as

$$R_N(T) \equiv \langle v_{NI}(t)v_{NI}(t+T)\rangle = \langle v_{NQ}(t)v_{NQ}(t+T)\rangle, \qquad (13a)$$

or

$$R_N(T) \equiv (K_R^2 K_1^2 R_i N_o / \tau) \rho(T) \tag{13b}$$

where $\rho(T)$ is a dimensionless correlation coefficient whose maximum value, unity, occurs at $T = 0$. Therefore, the sample voltage-squared average from the pre-averager is

$$<[\bar{v}_{NI}^j(t_\ell)]^2> = \sum_{-(M-1)/2}^{(M-1)/2} \sum_{-(M-1)/2}^{(M-1)/2} <v_{NI}(t_\ell - mT_r) v_{NI}(t_\ell - nT_r)>$$

$$\tag{14}$$

$$= \sum_{-(M-1)/2}^{(M-1)/2} \sum_{-(M-1)/2}^{(M-1)/2} R_N((m-n)T_r),$$

with an identical expression for the quadrature channel output.

The essence of the simplification of the above equation lies in the following argument. The voltages $v_{NI}(t)$ and $v_{NQ}(t)$ have bandwidths $B_R \simeq 1/\tau = 50$ kHz. The Fourier transform of any average spectrum with a nominal width B_R is a correlation function whose peak width (near $T = 0$) has a width $1/B_R \simeq \tau$; for time arguments considerably larger than τ, the correlation coefficient becomes negligibly small. Therefore, when $m \neq n$ in the above equation, we see that $(m-n)T_r \gg \tau$, and hence the double summation is negligible except for $m = n$. Thus Eq. (14) becomes

$$<[\bar{v}_{NI}^j(t_\ell)]^2> = <[\bar{v}_{NQ}^j(t_\ell)]^2> = R_N(0) \sum_{-(M-1)/2}^{(M-1)/2} 1 = MK_R^2 K_1^2 R_i N_o / \tau. \tag{15}$$

The actual noise signal $\bar{v}_{NI}^j(t_\ell) + i\bar{v}_{NQ}^j(t_\ell)$ at the input to the FFT processor is a random variable; however, the assumption that this noise is "white" or spectrally flat (on the average) means that the noise power $|V_N^j(\omega)|^2$ is spread uniformly across the spectral window of width $1/T_A$ after averaging. Hence, the average noise-power spectral-density height at the FFT output is given by

$$<S_N^j(\omega)> = \{<[\bar{v}_{NI}^j(t_\ell)]^2> + <[\bar{v}_{NQ}^j(t_\ell)]^2>\} \cdot T_A = 2MK_R^2 K_1^2 R_i N_o T_A / \tau. \tag{16}$$

Using the fact that we can define the power spectral density of the desired echo signal at its peak as $S_S^j(\omega_p) = |V_S^j(\omega_p)|^2 / T_I = M^2 T_I A_1^2$ $= M^2 T_I K_R^2 K_1^2 \cdot 2R_i P_R T_r / \tau$, we can form the signal-to-(average) noise ratio at the processor output as

$$S/N\Big|_p = \frac{|V_S^j(\omega_p)|^2}{\langle|V_N^j(\omega)|^2\rangle} = \frac{M^2 T_I K_R^2 K_1^2 \cdot 2R_i P_R T_r/\tau}{2M K_R^2 K_1^2 R_i N_o T_A/\tau} = \frac{P_R T_I}{N_o} , \tag{17}$$

where we have used the fact that $M = T_A/T_r$.

Hence we see that the signal-to-noise ratio at the output of our spectral processor, $S/N\big|_p$, is in fact identically that predicted by Eq. (5) as the optimum that one can expect for a matched receiver/processor. Therefore, our digital signal processing system does indeed provide the best possible processing of the signal from a moving target in the presence of white (random) noise.

5.1.3   Sea-Echo Radar Cross Section

In the previous section, we treated the radar target echo as a non-random CW signal (see Eqs. 7), as though it originated from a discrete target.   First-order sea echo in practice is a Gaussian random variable [Barrick and Snider, 1977].   Hence it makes sense to speak of the average sea-echo received power, or alternately, of the average sea-echo radar cross section.   Barrick [1972a, 1972b] shows that the average first-order sea-echo radar cross section, σ, is proportional to $\sigma^o A$, where A is the mean sea-surface area within the radar resolution cell and σ^o is the average sea-echo backscattering cross section per unit area.   The above references show that

$$\sigma^o = 2^6 \pi k_o^4 S(2k_o, 0), \tag{18}$$

where $S(K_x, K_y)$ is the average ocean waveheight directional (spatial) spectrum evaluated at spatial wavenumbers K_x, K_y, and k_o is the radar wavenumber. This expression is valid for vertically polarized backscatter at grazing incidence (i.e., for surface-wave geometries such as ours).   For $\sqrt{K_x^2 + K_y^2} > g/u^2$ (g = 9.81 m/s^2, u = wind speed, m/s), the waves with wavenumbers K_x, K_y are usually developed to their maximum possible heights, and an empirical expression found valid by oceanographers in this saturated region of the spectrum [Barrick, 1972b] is

$$S(K_x, K_y) = .005/[2\pi(K_x^2 + K_y^2)^2].$$

Using this expression in the above equation, we obtain $\sigma^o = 0.01$; this saturation condition at 30 MHz requires that > 2.8 m/s, or the waveheight be greater than approximately one-half foot, a condition that is nearly always true on the open sea.   Even when the sea is actually calmer than

this, some waves of the required scattering length (i.e., 5 meters) will always be present. If their heights are less than 6 inches, this simply means that the received echo signal will be proportionately weaker. For our analysis here, we will assume $\sigma^o = 0.01$ (a saturated condition).

The area within the resolution cell, A, we take to be that of a semi-circular annulus of width $c\tau/2$ ($c = 3 \times 10^8$ m/s, τ is the pulse width), and half-circumference πR (R being the range from the radar to the semi-circular range gate). Thus $A = \pi c\tau R/2$. For our first radar system, $\tau = 20$ μs, and hence the range-gate width, $c\tau/2$, is 3 km = 3×10^3 m. The total expression for the radar cross section of the sea — to be used in Eq. (6) — is

$$\sigma = 30\pi R, \qquad\qquad (19)$$

with σ having the dimensions of square meters and R in meters.

The equations stated in (5) and derived in (17) for signal-to-noise ratio of a moving target show a peak in the frequency domain whose height varies directly with, and width varies inversely with the spectral coherent integration time, T_I (or Fourier transform window time). These expressions are valid for any stationary target or target moving at a uniform radial velocity, whose echo signal can be expressed as a pure sinusoid, as assumed in Eq. (7). Barrick [1972a] has shown that this is true of sea echo to first order, in the absence of an underlying current shear. The entire principle of operation of the present system, however, assumes that the radial current-velocity component is not uniform around the semicircular ring, but varies according to some pattern (to be measured by the system). This "shear" will not produce a target signal at a single frequency, but will result in an echo signal with several frequencies (merging into a continuum) whose spread is related to the total variation in radial current velocity around the semicircle.

In order to study quantitatively the expected system signal-to-noise ratio under average conditions, we postulate the following model as a modification to the results of the preceding section, to account for current shear. In that section, we saw that the height of the spectral power peak was proportional to received power, P_R, times processing time T_I; the former quantity is proportional to the radar cross section of the target. The width of the spectral peak is inversely proportional to T_I. We now assume that the current shear broadens this peak to a width B_c, instead of the original width $1/T_I$. Since the total received backscattered power from the sea from the same semicircular ring remains the same, this means that the peak of the first-order sea-echo power spectrum must decrease proportionately. Thus, the signal-to-noise ratio decreases by a current-shear factor, F_{cs}, given by $F_{cs} = 1/(B_c T_I)$. Let us assume a current-shear radial-velocity variation across the semicircle from -100 cm/s to +100 cm/s (probably an extreme situation for coastal waters) in order to be somewhat conservative in our S/N calculations. Then at 30 MHz, $B_c = 0.4$ Hz. Then for our first-generation radar system with $T_I = 256$ seconds, we have $F_{cs} = 1/102.4 \simeq 0.01$.

51

5.1.4 System Signal-to-Noise Ratio vs. Range

At this point, we can re-write Eq. (6) for signal-to-noise ratio, using the parameters discussed in the preceding section.

$$S/N = \frac{P_{PT}\tau T_I}{T_r N_o} \cdot \frac{G_T G_R F^4}{(4\pi)^3 R^4} \sigma \cdot F_{cs} \, , \qquad \text{or} \qquad (20a)$$

$$S/N = \frac{P_{PT}\tau T_I}{T_r N_o} \cdot \frac{G_T G_R F^4 (.3)}{4^3 \pi^2 R^3} \, . \qquad (20b)$$

The system under design is to radiate a total of P_{PT} = 2400 W peak; also, τ = 20μs, T_r = 3 ms, and T_I = 256s. We use N_o = -184 dBJ at 30 MHz (or $N_o \simeq 4 \times 10^{-19}$ joules). The antenna gains used in the above used in the above equations must be referenced to free space, since the effect of ground imaging is included in the sea-echo radar cross section. For the receiving monopoles, this gives $G_R \simeq 0.75$. The transmitting antenna is more directional, and at its beam maximum, should have a "free-space" gain $G_T \simeq 3.28$ (based on the fact that the free-space Yagi half-wave dipole equivalent is to have a gain of 4 x 1.64).

Substituting all of these factors into Eq. (20), we obtain for our system:

$$S/N = 7.557 \times 10^{21} \times F^4/R^3 . \qquad (21)$$

Again, R is the range from the radar, given in meters. F is the dimensionless "Norton attenuation factor" for ground-wave propagation; it is unity at short ranges, but decreases (eventually exponentially) at longer ranges. It is also a function of frequency, surface conductivity, and surface roughness (sea state). It can be obtained from Barrick [1971]. We tabulate its average value below vs. range for sea water, a spherical Earth model, 30 MHz, and Sea State #2. Figure 28 also shows the S/N relationship graphically.

R(km)	F^4	S/N (decibels)*
5	.6210	105.7
10	.2512	92.8
20	$.3981 \times 10^{-2}$	65.8
30	$.3311 \times 10^{-3}$	49.7
40	$.4571 \times 10^{-4}$	37.3
50	$.9550 \times 10^{-5}$	27.6
60	$.2512 \times 10^{-5}$	19.4
70	$.7586 \times 10^{-6}$	12.2
80	$.2399 \times 10^{-6}$	5.5

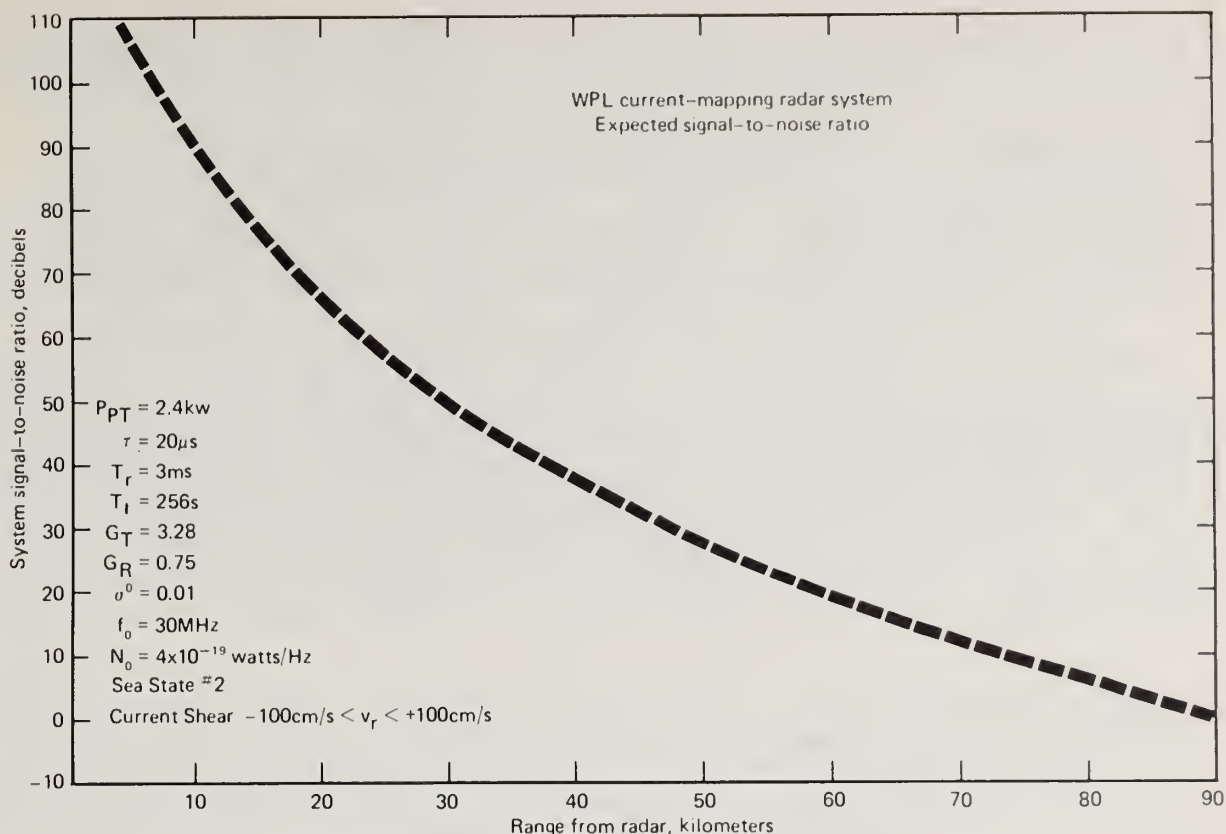* S/N is usually given in decibels, where in terms of absolute $(S/N)_a$, it is defined as $S/N = 10\log_{10}(S/N)_a$.

Figure graph content (axes and labels):

System signal-to-noise ratio, decibels (y-axis), Range from radar, kilometers (x-axis)

WPL current-mapping radar system
Expected signal-to-noise ratio

$P_{PT} = 2.4\,\text{kw}$
$\tau = 20\,\mu\text{s}$
$T_r = 3\,\text{ms}$
$T_I = 256\,\text{s}$
$G_T = 3.28$
$G_R = 0.75$
$\sigma^0 = 0.01$
$f_0 = 30\,\text{MHz}$
$N_0 = 4\times10^{-19}\,\text{watts/Hz}$
Sea State #2
Current Shear $-100\,\text{cm/s} < v_r < +100\,\text{cm/s}$

Figure 28.   Estimated signal-to-(external)noise ratio for current-sensing radar system under design.

Note that a positive average signal-to-noise ratio is maintained to somewhat beyond 80 km. Merely having an average signal-to-noise ratio greater than 0 dB (or greater than unity, absolute) does <u>not</u> mean system performance is adequate. With a <u>mean</u> S/N of 3 dB, for example, some non-negligible portion of the time the noise will exceed the signal, and will be mistaken for sea echo. Angle and Doppler values extracted when this happens will obviously be spurious, and will result in a degradation of system accuracy. Hence, it will be necessary — both by analyses/simulation studies and experiment — to determine a meaningful S/N threshold, lower than which no attempt will be made to process the received signal.

5.2   Optimization of Radar-Pair Spacing

In the preceding section, we calculated the signal-to-noise ratio of a single radar unit of our system as a function of distance or range from that unit. If one chooses a threshold signal-to-noise ratio, above which system operation is deemed satisfactory, one can from Fig. 28 find the maximum range coverage, R_c, corresponding to this threshold. For example, the maximum range corresponding to S/N $\simeq$ 10 dB is approximately $R_c \simeq 73$ km for the study parameters used in the preceding section. As far as the

53

construction of a map is concerned, radar-deduced current vectors can be
plotted only in the common region seen by both radar units; this area is
contained within overlapping circles of radius R_c centered on each site.
Let us assume the simple (and probably most common) site geometry illus-
trated in Fig. 29, where the two radar units are located on a straight
shoreline, separated by a spacing d_c; the common coverage area, A_c, above
the sea is shown shaded. The question to be addressed in this section
concerns the optimum site spacing for the coastal geometry assumed in Fig. 29.

There are undoubtedly many practical criteria that could be used to
optimize the site spacing, d_c, in terms of the coverage range, R_c. For the
sake of obtaining some initial feeling for this problem, we have chosen two
parameters and postulated a simple product relationship between them to
define an optimization curve. The first parameter is A_c, the common coverage
area. One would like this to be as large as possible (in terms of a given
R_c) so that currents over the widest possible area would be observed for a
given coastal measurement. Obviously, this is obtained as the two sites
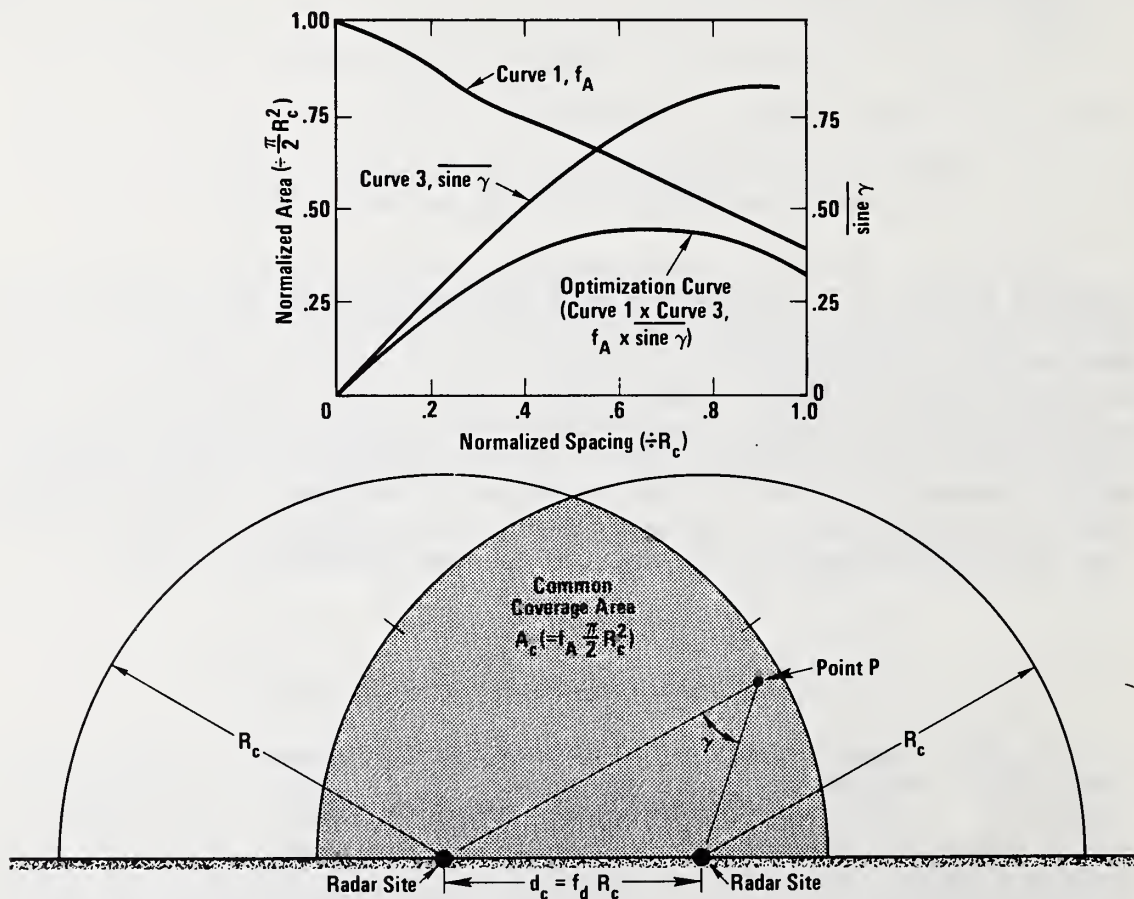move together ($d_c \to 0$), in which case $A_c \to (\pi/2)R_c^2$. A plot of normalized

*Figure 29.   Geometry and optimization criteria for
arriving at site spacing, d_c.*

common area (i.e., $A_c \div (\pi/2)R_c^2$) vs. normalized site separation (i.e., $d_c \div R_c$) is shown as f_A at the top of Fig. 29.

The single criterion of maximizing the area, however, is inadequate. As $d_c \to 0$ and the sites move together, both sites sample the <u>same</u> radial component of current velocity, and hence it is no longer possible to obtain the <u>total</u> current vector. Two vector components for each grid point having a known angle, γ, between them are necessary to obtain the total vector. As one might suspect, even when d_c is finite but very small, the angle γ between the two radial current components at each point in the scattering area is small, and the angular accuracy in obtaining the total current vector will be poor. Best angular accuracy for the total current vector at a given point will be obtained when γ is near 90° (or $\sin \gamma$ is near unity); this can be realized only when d_c is not too small. One can define an "average" $\sin \gamma$ over every point in the coverage area as follows:

$$\overline{\sin \gamma} = \int\int_{A_c} \sin \gamma \, dA, \qquad (22)$$

where dA is an element of area at Point P and γ is the angle between the two radial lines, shown in Fig. 29. This integral is best done numerically, and the curve for this average is shown at the top of Fig. 29 as a function of normalized site spacing. The maximum in this curve appears at $d_c/R_c \simeq 0.9$, and the curve decreases to zero as $d_c \to 0$, as it should.

The optimization criterion that is used here is the product of the common coverage area, A_c, and the size of the measured current-vector angle, γ. Thus the "optimization curve" is merely the product of Curve 1 and Curve 3 vs. d_c; this is shown at the top of Fig. 29. The maximum in this curve is broad, but indicates that the best spacing is $d_c \sim 0.7\ R_c$.

This criterion and optimization curve should in practice serve as a general guideline only. Since the maximum is broad, one should consider other factors in choosing the specific separation in a given case such as the coastal topography, logistic conveniences at various site locations, and the desirability of increasing (somewhat) the common coverage area so that certain areas of particular oceanographic interest will be included.

5.3 Accuracies vs. Noise and Signal Statistics

5.3.1 Azimuthal (Direction-of-Arrival) Accuracy vs. Noise

The manner in which a single radar unit of the present system determines the angle-of-arrival (i.e., azimuth) of the incoming signal is analogous to radio (phase) direction finders. The original concept of Crombie et al., [1970] and the first design we considered called for two receiving antennas separated by a distance d. By measuring the phase difference for a signal

arriving at the two antennas from an angle α_s with respect to the perpendicular to the line joining the two antennas (the latter line referred to as the antenna baseline), one can uniquely determine α_s (so long as $d < \lambda/2$). The relationship between this phase difference, Φ_s, and α_s is simply $\Phi_s = k_o d \sin \alpha_s$, where $k_o = 2\pi/\lambda$ is the radar wavenumber.

It is well known that when noise is present along with the desired signal whose angle-of-arrival is sought, the apparent signal angle — as determined from the phase difference — will be in error. The lower the singal-to-noise ratio, the worse will be the error. Conversely, the direction-of-arrival accuracy increases with increasing signal-to-noise ratio. The purpose of this section is to study this relationship for a given signal and noise model. Quite obviously, the exact relationship will depend to some extent on the precise noise and signal models used (as well as upon whether two or three receiving antennas are employed), but none-theless a feeling for the angular accuracy in general can be obtained from the model to be considered below.

We consider a CW plane-wave signal arriving from an angle α_s, having a constant, non-random amplitude. Added to this is a noise signal whose average power is distributed uniformly in angle* (i.e., the noise is azimuthally isotropic). The total voltages at the two antennas (a and b) can then be written

$$v_a(t) = s(t, \alpha_s) + n(t) = s(t, \alpha_s) + \int_o^{2\pi} \hat{n}(t,\alpha)d\alpha, \qquad (23a)$$

$$\text{and} \quad v_b(t) = s(t-(t-(d/c)\sin \alpha_s, \alpha_s) + \int_o^{2\pi} \hat{n}(t-(d/c)\sin \alpha, \alpha)d\alpha, \qquad (23b)$$

where antenna "a" is taken as the reference antenna. The Fourier transforms of these signals now become:

$$V_a(\omega) = S(\omega) + N(\omega) = S(\omega) + \int_o^{2\pi} \hat{N}(\omega,\alpha)d\alpha, \qquad (24a)$$

$$\text{and} \quad V_b(\omega) = e^{j (d/c)\sin\alpha_s} S(\omega) + \int_o^{2\pi} \hat{N}(\omega,\alpha) e^{j (d/c)\sin \alpha} d\alpha, \qquad (24b)$$

where $S(\omega)$ and $\hat{N}(\omega,\alpha)$ are the Fourier transforms of $s(t,\alpha_s)$ and $\hat{n}(t,\alpha)$, respectively.

_____

* The case in which the noise arrives from one (or more) discrete direction, α_n, can be examined also; in this situation the unwanted signal is usually termed interference. The angular error in resolving the signal direction in this case is actually easier to analyze than the isotropic noise model, but will not be undertaken here.

56

Average power spectral densities can be defined for both signal and noise as follows:

$$S(\omega) = \lim_{T \to \infty} \frac{\langle S_T(\omega) S_T^*(\omega) \rangle}{T} \quad , \tag{25a}$$

$$N(\omega) = \lim_{T \to \infty} \frac{\langle N_T(\omega) N_T^*(\omega) \rangle}{T} \quad , \tag{25b}$$

$$\hat{N}(\omega,\alpha)\delta(\alpha-\alpha') = \lim_{T \to \infty} \frac{\langle \hat{N}_T(\omega,\alpha) \hat{N}_T^*(\omega,\alpha') \rangle}{T} \quad , \tag{25c}$$

where the subscript T refers to a "finite-length" Fourier transform over limits $-T/2$ to $T/2$ (instead of $-\infty$ to ∞). In practice, the Fourier transform is computed numerically over a finite "window" anyway; so long as T is large compared with the period of the carrier frequency, the limiting processes are unnecessary.

The last equation above is equivalent to a Fourier-Stieltges angular noise representation; it says in effect that a noise voltage coming from direction α is uncorrelated with noise arriving from direction α'. This is a realistic assumption for natural, random noise processes distributed spatially about the antenna. The Dirac-delta function on the left side of the equation causes the left side to vanish when $\alpha \neq \alpha'$.

At this point, we define the cross-correlation (or cospectrum) of the signal at antenna "a" with that at antenna "b":

$$C(\omega) \equiv \lim_{T \to \infty} \frac{\langle V_{aT}(\omega) V_{bT}^*(\omega) \rangle}{T} \equiv |C(\omega)| e^{-j\Phi(\omega)} . \tag{26}$$

Upon substituting Eqs. (24) into this definition and using the Eqs. (25), we obtain

$$|C(\omega)| e^{-j\Phi(\omega)} = S(\omega) e^{-j\omega(d/c)\sin\alpha_s} + \int_0^{2\pi} \hat{N}(\omega,\alpha) e^{-j\omega(d/c)\sin\alpha} \, d\alpha . \tag{27}$$

In obtaining this expression, we have used the fact that the signal and noise voltages are uncorrelated, and hence their cross-product terms vanish in the averaging process. Also, if the signal is actually monochromatic at frequency ω_o, we can replace ω by ω_o in the first term; in the exponential, therefore, we have $\omega(d/c) = \omega_o(d/c) = k_o d$. If the noise has been narrow-band-filtered about ω_o and is spectrally flat (or "white")

57

across this filter bandwidth, we can make this substitution for ω in the second term also. Finally, we postulated that the signal amplitude was a non-random constant; this does not affect the spectrum $S(\omega)$, for the average of a constant is the constant itself.

The assumption that the average noise is isotropic in angle means that $\hat{N}(\omega_o,\alpha)$ is not a function of α; hence we can make the substitution $\hat{N}(\omega_o,\alpha) = N(\omega_o)/2\pi$ and remove this factor from the integrand. The remaining integral containing only the exponential then gives rise to the zero-order Bessel function. Hence we have

$$|C(\omega_o)|e^{-j\Phi(\omega_o)} = S(\omega_o)e^{-jk_o d \sin\alpha_s} + N(\omega_o)J_o(k_o d). \qquad (28)$$

Since $S(\omega)$ and $N(\omega)$ are pure real quantities, we can write the phase difference $\Phi(\omega_o)$ from the averaged cospectrum above. Note that in the absence of noise, this phase is exactly the expression we discussed at the outset of this section in terms of the signal arrival direction α_s. With noise, however, Φ depends upon the average signal-to-noise ratio $(S/N \equiv S(\omega_o)/N(\omega_o))$ also. Thus we can write

$$\Phi(\omega_o) = \tan^{-1}\frac{\sin(k_o d \sin\alpha_s)}{\cos(k_o d \sin\alpha_s) + J_o(k_o d)/(S/N)} \equiv k_o d \sin\alpha_e, \qquad (29)$$

where α_e is the estimated direction-of-arrival and α_s is the true direction-of-signal-arrival. The angular estimation error is then $\varepsilon = \alpha_e - \alpha_s$.

In order to obtain a feeling for the dependence of ε upon S/N, we choose several parameter values for α_s and $k_o d$ for the above model and plot ε vs. S/N. These curves are shown in Fig. 30.

The curves plotted from Eq. (29) indicate that — for the signal and noise model examined here — the mean angular error in estimating direction of arrival is always less than 3° for S/N > 10 dB, but this angular error increases rapidly as S/N drops below 10 dB. This is consistent with other analyses on this subject also. While the system being implemented differs from the model analyzed here (both in the fact that three antennas are used instead of two and in the fact that the estimated angle is extracted before averaging), the results obtained here are expected to be generally applicable to our system also. More precise angular error analyses for our system will be performed in a subsequent report; such an analysis must of necessity be done digitally, using the actual system software along with Monte-Carlo techniques for signal and noise. An example of a simulated current plot using these techniques is shown in the next section.
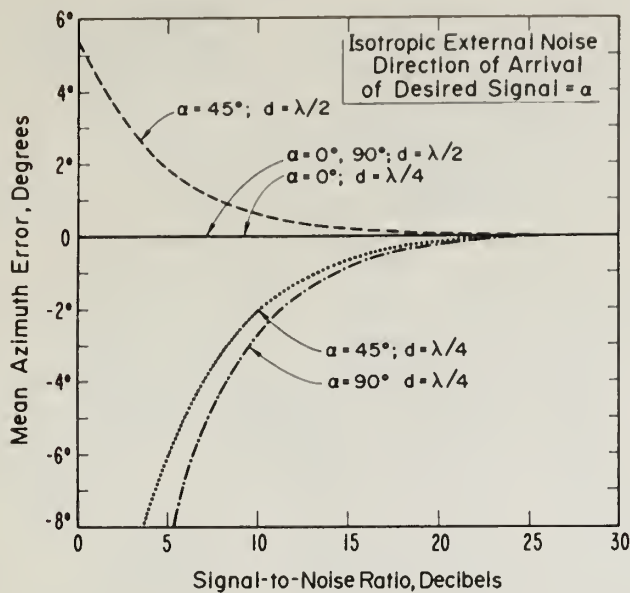
Figure 30. *Mean azimuth-angle mea-
surement errors for two-antenna
system and various signal arrival
directions, α_s, and antenna
spacings, d.*

5.3.2 Simulation of Current Map Using Actual Data-Processing Software

As mentioned in the preceding section, it is impossible to develop a
closed-form mathematical model for our current-vector errors for several
reasons: (i) Thresholding is used to eliminate data points originating at
low signal-to-noise ratio values; this is a nonlinear process making the
analysis very complex. (ii) The equations giving the two angles-of-arrival
in a three-antenna system (i.e., Eqs. 1-3) are quite involved transcendental
relationships. (iii) Averaging is done after angular extraction from the
signals. (iv) This averaging is done on the Doppler frequency (or radial
current velocity), rather than on the azimuth angle. Hence the only practi-
cable way of obtaining a feeling for current-vector errors is by simulating
the random sea-echo signals and noise signals, employing the Doppler-shift
distribution on the sea-echo signal produced by a predetermined current
pattern.

Another reason for doing such simulations is to check out the system
data-processing software before actually operating in the field. In this
manner, "bugs" in the programming can be found in the laboratory. Also, by
varying the current-pattern geometries and system parameters, we can anti-
cipate trouble areas in system operation before going into the field, and
modifications can be made where appropriate.

In Fig. 25, two possible sets of signals were shown at the upper left
as inputs to the data-processing software. The first set represents actual
sea-echo signals as they would pass through the receiver in the field and
exist in digital time-series form at the input to the FFT. The second set
are simulated signals of the type being discussed here for laboratory
studies and analyses. Both sets of signals pass through the same software,
and hence the software (with the underlying mathematical processes and
attendant accuracies) can be checked with properly simulated signals.

An entirely separate computer program is being used to generate simulated signal data tapes for use with the system software. These simulated signals for a given range gate consist of two components: (i) the random sea-echo signals, and (ii) random noise signals. The random sea-echo signal for the I and Q channel time series is assumed to originate from $180°/\Delta\alpha$ different scattering directions. Typically we have used $\Delta\alpha = 1°$, meaning that the sea-echo is assumed to be different every degree in azimuth over a 180° semicircle. This difference manifests itself in three ways: (i) The I and Q channel amplitudes X_{si} and Y_{si} of the signals from each direction, α_i ($\alpha_i = i\Delta\alpha$) are assumed to be uncorrelated Gaussian random variables. (ii) The frequency of the signal is assumed to be $f_B + f_{Di}$, where f_B is the first-order Bragg-scatter frequency and f_{Di} is the Doppler frequency due to the radial velocity component of the assumed current pattern at the i-th azimuthal point around the range semicircle. (iii) The phase of the signal is $(\ell-1)k_o d \sin(\frac{i\pi\Delta\alpha}{180°})$, where $\ell = 1$, 2, or 3 for each of the three receiving antennas, and $i\Delta\alpha = \alpha_i$ is the angle in degrees of the signal with respect to the perpendicular to the antenna baseline. Hence the total I and Q channel sea-echo signal at a given time t_j is the summation of $180°/\Delta\alpha$ terms, each representing the signal from a different azimuthal direction $i\Delta\alpha$.

The simulated noise signal is also the summation of $180°/\Delta\alpha$, I and Q channel terms. However, at each sampling time, t_j, these amplitudes, X_{Nij} and Y_{Nij}, are assumed to be uncorrelated Gaussian random variables (as well as uncorrelated for each azimuthal direction as represented by different i). This has the effect of giving the noise power a bandwidth $B_N \simeq 0.5/(t_{j+1} - t_j)$, where $t_{j+1} - t_j$ is the time between the time-series signal samples at the output of the pre-averaging circuit and input to the FFT. Thus the average noise power will be spread uniformly over the output FFT window from $-B_N$ to $+B_N$ Hz. The noise signal originating from each of the α_i different azimuthal directions is given the phase factor discussed in (iii) of the preceding paragraph, corresponding to the receiving antenna element being considered. This latter fact and the independence of the X_{Nij} over i has the physical meaning that the noise is essentially isotropic in direction, i.e., the noise originates with equal average power levels from all directions.

Using these models for simulated sea-echo and noise signals, we have exercised the system software for different current patterns and signal parameters. Figure 31 is an example of one such early simulation. The input current pattern employed here was a one-half-knot uniform field flowing away from a line joining two sites (40 km apart) straddling Yakutat Bay in Alaska. Had there been no noise or sea-echo signal randomness, the output pattern would have had all of the arrows straight and of the same length. For this particular simulation, the following additional assumptions were made: (i) Frequency is 30 MHz. (ii) Only one FFT sample was employed (i.e., one 256-second run only). (iii) The antenna baselines at the two sites lie parallel to the line shown joining the sites. (iv) The signal-to-noise ratio defined as $<X_{si}^2>/<X_{Nij}^2>$ is 20 dB. This corresponds to an
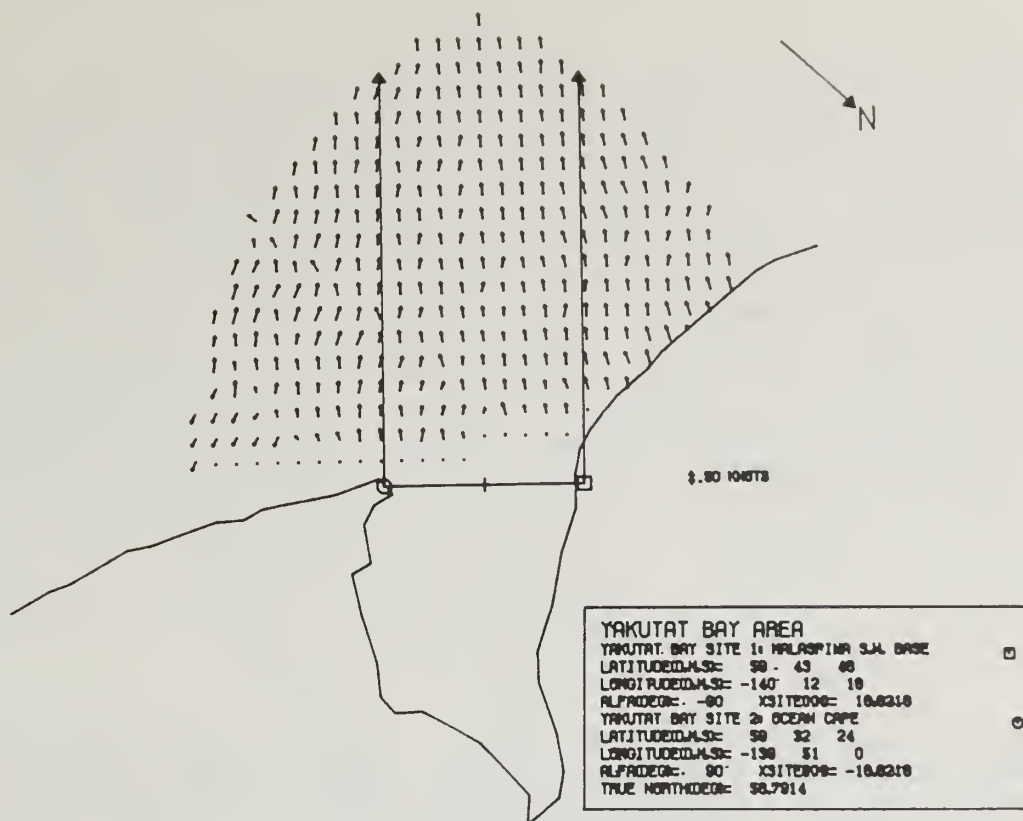
60

*Figure 31.   Current-map simulation based on input,
uniform offshore current field.*

actual signal-to-noise ratio (i.e., average first-order signal spectral
peak to average noise level) of $\sim$ 33 dB.   (v) Only those data points cor-
responding to total signals exceeding a 10-dB threshold below the first-
order sea-echo signal maximum were retained.   (vi) A rectangular weighting
window at the FFT input was used, giving rise to a (sinx/x) pattern at the
output; this gives rise to considerable "spillover" between data at adjacent
Doppler frequency points, and hence is a type of distortion. (vii) The same
azimuthal signal and noise signals were used for each range gate.

Thus the parameters employed for this early simulation are by no means
optimum.   Improvements in the data-processing software are being made
constantly, and are presently being tested against more realistic current
patterns.   System accuracies vs. various averaging, interpolation, and
curve-fitting techniques will be quantitatively established through such
simulations, in addition to vector plots — such as that in Fig. 31 — for
more qualitative, subjective judgments.

One feature of the simulation represented by Fig. 31 worth special
note is the double-valued nature of the radial current (and hence Doppler
frequency) vs. azimuth angle.   That is, the radial current velocity is the
same at -α as at +α for this pattern.   Using a two-antenna system such as
that of Crombie et al., [1970] would <u>not</u> have permitted the resolution of
this ambiguity, whereas our three-antenna method handles this situation
properly.

61

6. SUMMARY

We have developed a transportable HF radar system that measures current velocities by actually observing simple (first-order) scatter from the ocean waves, which in effect serve as a "tracer" for the underlying currents. Employing simple, easily erectable antennas on the beach, our system can obtain the angular direction of arrival of the echo signals by phase comparisons among three short receiving antennas. In addition to theory and analyses — which showed that the concept should work — several research experiments done over the past several years have demonstrated the soundness of the underlying techniques. Therefore, we entered our development program with the objectives of constructing, testing, and operating a relatively inexpensive, self-contained van-transportable system that could produce a useful, readily interpretable output in the field. Our feasibility studies showed that such a two-unit system could in fact be constructed, with the following desirable characteristics: (i) near-coastal area covered, $\sim$ 5000 km^2; (ii) spatial (grid) resolution, 3 km x 3 km; (iii) current-velocity accuracy, $\sim$ 5 cm/s; (iv) only currents within $\sim$ 1 meter of surface are observed; (v) total transmitted average power < 50 watts; (vi) additional two-station pairs could be commercially manufactured for $\sim$ $75,000.

Undertaking development and implementation of our system with financial support from NOAA/ERL, BLM, the U.S. Coast Guard, and ERDA, we have designed and constructed the following major system hardware components in-house: (i) the A/D Hardware and System Timing Module; (ii) the Semiconductor Mass-Storage Module; (iii) the FFT Processor (fast-Fourier transform); (iv) the Transmitter Driver; (v) the Transmitter Power Amplifiers; (vi) the Receiving Antennas; (vii) the Transmitting Antennas; (viii) and the many necessary interfaces between components. Our design of the transmitting antennas has been based upon a contracted study done for us by Lawrence Livermore Laboratories, in which they digitally optimized a Yagi monopole array to have a specified moderate directional gain and an input impedance of 50Ω. Major hardware elements specified but purchased outside include the following: (i) the Linc-Tape Recorder; (ii) the PDP 11/04 Minicomputer; (iii) the Keyboard/Printer Terminal; (iv) the Graphic System, including a video (scope) monitor and an incremental, digital pen plotter; (v) the Radar Receiver System; (vi) the fiberglass mounting cases. All of the components (both in-house constructed and purchased) are on hand, and are being assembled and integrated into the system field cases.

All of the normal system operations during a data run — along with the system software functions — are controlled by a timing device. This is the source for not only the transmitted radar frequency, the pulse train and sampling pulses, and RF switching, but also the commands that control the software task sequencing required to process the data in real time. The fundamental software package that interfaces between the minicomputer hardware and the required system functions is called the operating system; the particular system used here is RSX11S, supplied by the Digital Equipment Corporation (the manufacturer of the minicomputer). Most of the "control" software has already been written; this term describes the programs which permit the operator and computer to control all of the operation of the radar system. The data-processing software has been written in FORTRAN and

checked out with simulated radar signals; this software processes the received radar signals after digitization to produce a current-map output.

System analyses have been completed that trace the signal flow through the digital system and compute the signal-to-noise ratio. These analyses show that an adequate sea-echo signal-to-noise (> 10 dB) ratio should be attainable to a distance of 70 kilometers from each station. On the basis of this distance, an optimization study has shown that for a straight coastline, a desirable site separation would be near 40 km. Error analyses show that for signal-to-noise ratios greater than 10 dB, azimuthal position errors should be less than 3°. Simulations using random sea-echo and noise signals are being conducted to check out, exercise, and improve the data-processing software in the laboratory, before operating in the field. These simulations thus far reaffirm our expectation that rms current-velocity errors will not exceed 5 cm/s.

7. ACKNOWLEDGMENTS

8. REFERENCES

Barrick, D. E., (1971), Theory of HF/VHF propagation across the rough sea, Parts I and II, Radio Science, Vol. 6, pp. 517-533.

Barrick, D. E., (1972a), First-order theory and analysis of MF/HF/VHF scatter from the sea, IEEE Transactions on Antennas and Propagation, Vol. AP-20, pp. 2-10.

Barrick, D. E., (1972b), Remote sensing of sea state by radar, Chapter 12 in Remote Sensing of the Troposphere, edited by V. E. Derr, U.S. Govt. Printing Office.

Barrick, D. E., J. M. Headrick, R. W. Bogle, and D. D. Crombie, (1974), Sea backscatter at HF: interpretation and utilization of the echo, Proc. IEEE, Vol. 62, pp. 673-680.

Barrick, D. E., and J. B. Snider, (1977), The statistics of HF sea-echo Doppler spectra, accepted for publication in IEEE Transactions on Antennas and Propagation.

C.C.I.R. (International Radio Consultative Committee) Report No. 322 (1964) "World Distribution and Characteristics of Atmospheric Radio Noise", International Telecommunication Union, Geneva, M64, 78 pp.

Cook, C. E., and M. Bernfeld, (1967), Radar Signals. An Introduction to Theory and Application, Academic Press, New York, 531 pp.

Crombie, D. D., (1955), Doppler spectrum of sea echo at 13.56 Mc/s, Nature Vol. 175, pp. 681-682.

Crombie, D. D., J. M. Watts, and W. M. Beery, (1970), Spectral characteristics of HF ground wave signals backscattered from the sea, Electromagnetics of the Sea, AGARD Conference Proceedings No. 77. National Technical Information Service, Springfield, Virginia; Accession No. AD 716 305.

Skolnik, M. I., (1962), Introduction to Radar Systems, McGraw-Hill, New York, pp. 3-5 (648 pp.)

Stewart, R. H., and J. W. Joy, (1974), HF radio measurements of surface currents, Deep Sea Research, Vol. 21, pp. 1039-1049.

Wait, J. R., (1966), Theory of HF ground wave backscatter from sea waves, J. Geophys. Res., Vol. 71, pp. 4839-4842.

Environmental Research
LABORATORIES

The mission of the Environmental Research Laboratories is to study the oceans, inland waters, the lower and upper atmosphere, the space environment, and the Earth, in search of the understanding needed to provide more useful services in improving man's prospects for survival as influenced by the physical environment. The following laboratories contribute to this mission.

MESA — *Marine EcoSystems Analysis Program Office* Plans and coordinates regional programs of basic and applied research directed toward the solution of environmental problems which involve the functioning, health and restoration of marine ecosystems

OCSEA — *Outer Continental Shelf Environmental Assessment Program Office.* Plans and directs assessments of the primary environmental impact of energy development along broad areas of the outer continental shelf of the United States, coordinates related research activities of federal, state and private institutions.

W/M — *Weather Modification Program Office* Plans and directs ERL weather modification research for precipitation enhancement and severe storms mitigation, operates ERL's research aircraft

NHEML — *National Hurricane and Experimental Meteorology Laboratory.* Develops techniques for more effective understanding and forecasting of tropical weather Research areas include hurricanes and tropical cumulus systems, experimental methods for their beneficial modification

RFC — *Research Facilities Center* Provides aircraft and related instrumentation for environmental research programs. Maintains liaison with user and provides required operations or measurement tools, logged data, and related information for airborne or selected surface research programs

(CIRES) — *Theoretical Studies Group.* Provides NOAA participation in the Cooperative Institute for Research in Environmental Sciences (CIRES), a joint activity with the University of Colorado Conducts cooperative research studies of a theoretical nature on environmental problems

AOML — *Atlantic Oceanographic and Meteorological Laboratories.* Research areas include geology and geophysics of ocean basins and borders, oceanic processes, sea-air interactions and remote sensing of ocean processes and characteristics (Miami, Florida)

PMEL — *Pacific Marine Environmental Laboratory* Research areas include environmental processes with emphasis on monitoring and predicting the effects of man's activities on estuarine, coastal, and near-shore marine processes (Seattle, Washington)

GLERL — *Great Lakes Environmental Research Laboratory* Research areas include physical, chemical, and biological limnology lake-air interactions, lake hydrology lake level forecasting and lake ice studies (Ann Arbor, Michigan)

GFDL — *Geophysical Fluid Dynamics Laboratory* Research areas include dynamics and physics of geophysical fluid systems development of a theoretical basis, through mathematical modeling and computer simulation, for the behavior and properties of the atmosphere and the oceans (Princeton, New Jersey)

APCL — *Atmospheric Physics and Chemistry Laboratory* Research areas include processes of cloud and precipitation physics chemical composition and nucleating substances in the lower atmosphere, laboratory and field experiments toward developing feasible methods of weather modification

NSSL — *National Severe Storms Laboratory* Research is directed toward improved methods of predicting and detecting tornadoes squall lines, thunderstorms, and other severe local convective phenomena (Norman, Oklahoma)

WPL — *Wave Propagation Laboratory* Research areas include theoretical research on radio waves optical waves, and acoustic gravity waves experimental research and development on new forms of remote sensing

ARL — *Air Resources Laboratories* Research areas include diffusion, transport, and dissipation of atmospheric contaminants development of methods for prediction and control of atmospheric pollution geophysical monitoring for climatic change (Silver Spring, Maryland)

AL — *Aeronomy Laboratory* Research areas include theoretical, laboratory rocket and satellite studies of the physical and chemical processes controlling the ionosphere and exosphere of the Earth and other planets, and of the dynamics of their interactions with high-altitude meteorology

SEL — *Space Environment Laboratory* Research areas include solar-terrestrial physics service and technique development in the areas of environmental monitoring and forecasting

NATIONAL OCEANIC AND ATMOSPHERIC ADMINISTRATION
BOULDER, COLORADO 80302